Frequency Limitation for Triaxial Induction Tools and Dielectric Tools in 1-D Multi-Layered Transverse Isotropic Formation

A Thesis

Presented to

the Faculty of the Department of Electrical and Computer Engineering

University of Houston

In Partial Fulfillment

of the Requirements for the Degree

Master of Science

in Electrical and Computer Engineering

By

Aobo Jin

May 2016

Frequency Limitation for Triaxial Induction Tools and Dielectric Tools in 1-D Multi-Layered Transverse Isotropic Formation

Aobo Jin

Approved:

Chair of the Committee
David R. Jackson, Professor
Electrical and Computer Engineering

Committee Members:

Ji Chen, Professor
Electrical and Computer Engineering

Jiefu Chen, Professor
Electrical and Computer Engineering

Driss Benhaddou, Professor
Engineering Technology

Suresh K. Khator, Associate Dean
Cullen College of Engineering

Badrinath Roysam, Professor and Chair
Electrical and Computer Engineering

Acknowledgments

First, I would like to sincerely thank my advisors, Dr. Richard C. Liu and Dr. David R. Jackson, for their patience and valuable guidance during this thesis.

Second, I am grateful to my committee members, Dr. Ji Chen, Dr. Jiefu Chen and Dr. Driss Benhaddou for their constructive suggestions and invaluable help and for taking the time to serve on my thesis committee. I would like also to express my great thanks to Dr. Ji Chen and Dr. Jiefu Chen for sharing their knowledge about dielectric tools. I would like to especially thank Dr. Hanming Wang for his generous help and for providing me several with related materials.

Third, I owe thanks to my labmates in Well Logging Lab: Zhijuan Zhang, Boyuan Yu, Yinxi Zhang, Bo Gong, Jing Wang and Mengsu Zhou. They provided considerable assistance during my research. I really enjoyed collaborating with them.

Finally, I would like to thank my parents and family for their continuous support and encouragement.

Frequency Limitation for Triaxial Induction Tools and Dielectric Tools in 1-D Multi-Layered Transverse Isotropic Formation

An Abstract

of a

Thesis

Presented to

the Faculty of the Department of Electrical and Computer Engineering

University of Houston

In Partial Fulfillment

of the Requirements for the Degree

Master of Science

in Electrical and Computer Engineering

By

Aobo Jin

May 2016

Abstract

Triaxial induction tools are used in well logging to efficiently measure formation anisotropy including reservoir rocks that show anisotropy, such as thin laminated reservoirs.

Dielectric tools are mainly used to detect fresh water and carbonate. They are vital in distinguishing thinly laminated shale oil/gas detection. Dielectric tools have higher working frequency than triaxial induction tools.

In this thesis, an analytical method is used to simulate the responses of triaxial induction tools in one-dimensional multi-layered transverse isotropic formation with both the borehole and invasions neglected.

Dielectric tools have the same basic formulations as triaxial induction tools except there only have two directions. Given the wide use of dielectric tools in the industry, having a simulation method that can simulate dielectric tools with speed and accuracy is important. Thus, frequency limitation for the simulation method is studied in this thesis to determine if this simulation method can simulate dielectric tools.

Table of Contents

List of Figures

List of Tables

Chapter 1 Introduction

1.1 Background

In the resistivity market, the induction tool has been mainly produced because of its accuracy in detecting formation resistivity in drilling environments. One transmitter coil and one or two receiver coils arranged with their axis orientated along the axis of the borehole can be found in a traditional induction logging tool, and this tool has no sensitivity to resistivity anisotropy, which means traditional induction tool cannot tell the difference between thick low-resistivity bed and laminated thin-bed zone. Given that the resistivity in the transverse direction is isotropic, it is transverse isotropy. Measuring thin laminated reservoirs accurately is critical because numerous thick-layered oil reservoirs are getting exhausted.

1.1.1 Triaxial Induction Logging

A triaxial induction tool is an emerging tool with both traditional *z* and *x*-*y* antennas as transmitters and receivers. This tool consists of three orthogonal transmitters and three orthogonal receivers, as shown in Figure 1.1.

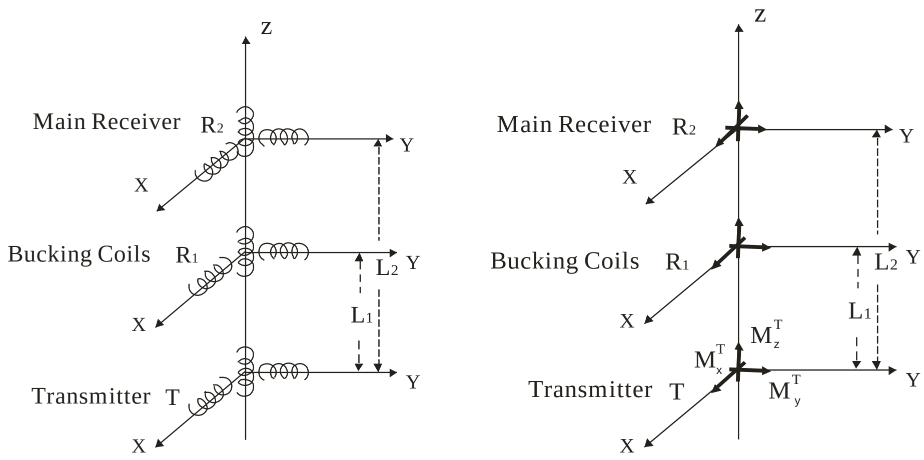

(a) Basic structure of a triaxial induction tool (b) Equivalent dipole model

Figure 1.1. Basic structure of a triaxial induction tool and its equivalent dipole model.

In a triaxial induction tool, each transmitter and receiver can be treated as point magnetic dipoles because the coils are assumed to be sufficiently small. Three components of the induced field exist at each receiver. Thus, nine components will be produced as

$$\mathbf{H} = \begin{bmatrix} H_{xx} & H_{xy} & H_{xz} \\ H_{yx} & H_{yy} & H_{yz} \\ H_{zx} & H_{zy} & H_{zz} \end{bmatrix},$$

where the first subscript corresponds to the transmitter index and the second corresponds to the receiver index. Therefore, H_{ij} denotes the magnetic field received by the j-directed receiver coil excited by the i-directed transmitter coil.

Formation anisotropy responds to different components in tool transmitter-receiver combinations. Therefore, the triaxial tool can measure formation resistivities with anisotropy.

1.1.2 Dielectric Tool

Dielectric tools are single frequencies around 1 GHz with one or two transmitters and one or two receivers. Transmitters and receivers are modeled as unit moment magnetic dipoles in this thesis. The array dielectric logging tool is known for its extensive applications because it possesses multiple frequency channels and various combinations of transmitter and receiver sets. The array dielectric logging tool that comprises two transmitting antennas and eight receiving antennas symmetrically surrounding the transmitting antennas is shown in Figure 1.2. Each antenna is a cross-dipole offering collocated normal magnetic dipoles working in longitudinal and transversal modes.

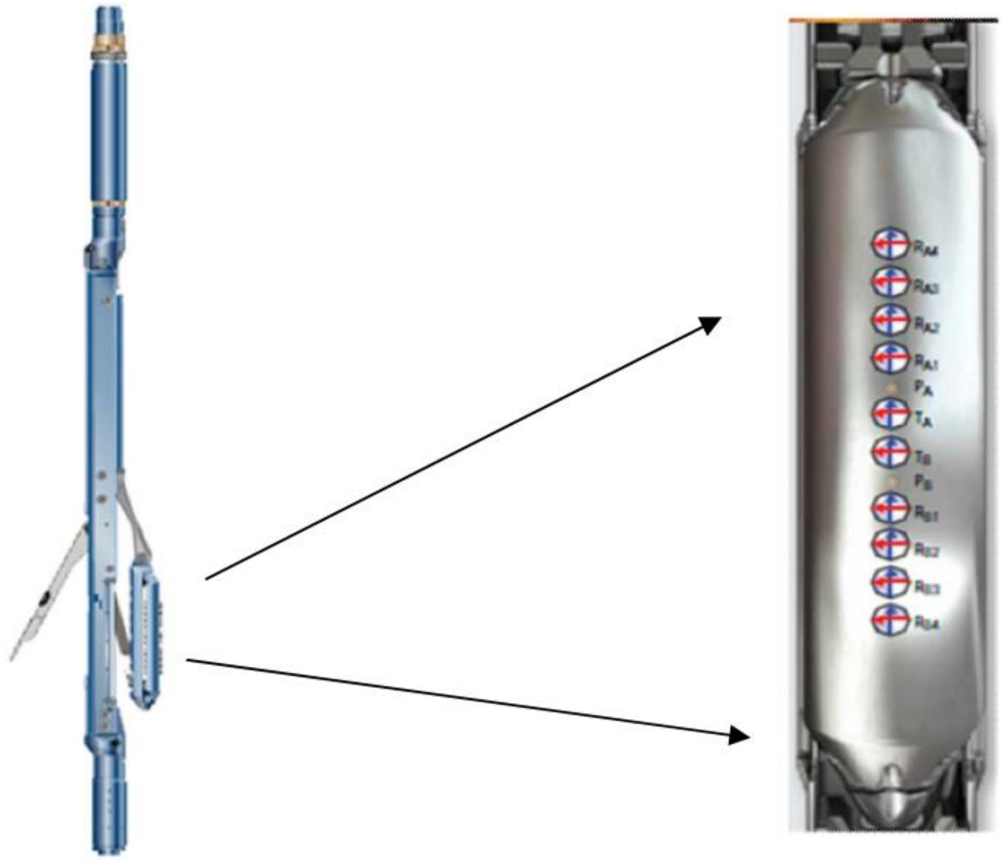

Figure 1.2. Schematic of dielectric logging array.

1.1.3 1-D Multi-Layered Transverse Isotropic Formation

A transversely isotropic material is one with physical properties, that are symmetric about an axis that is normal to a plane of isotropy. The formation properties are the same in all directions.

Figure 1.3 shows the basic structure of transverse isotropy. In this paper, we consider a 1-D multi-layered transverse isotropic formation with both the borehole and invasions neglected.

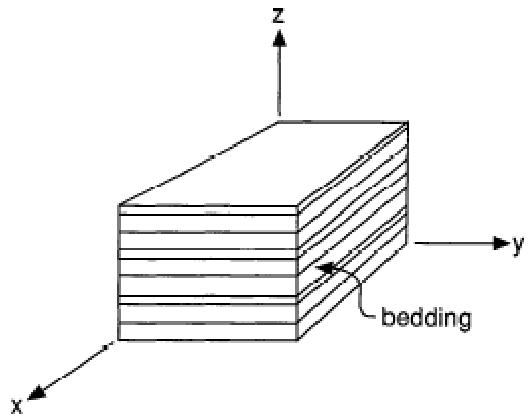

Figure 1.3. Transverse isotropy.

Figure 1.4 shows the thin laminated reservoir.

Figure 1.4. Thin laminated reservoir.

The electrical conductivity and permittivity of a medium are positive-definite symmetric second-rank tensors. For a transverse isotropic medium, the conductivity and permittivity tensors will be

$$\boldsymbol{\sigma} = \begin{bmatrix} \sigma_h & 0 & 0 \\ 0 & \sigma_h & 0 \\ 0 & 0 & \sigma_v \end{bmatrix} \tag{1}$$

and

$$\boldsymbol{\varepsilon} = \begin{bmatrix} \varepsilon_h & 0 & 0 \\ 0 & \varepsilon_h & 0 \\ 0 & 0 & \varepsilon_v \end{bmatrix}, \tag{2}$$

where σ_h and ε_h are the horizontal components of the conductivity and permittivity respectively. σ_v and ε_v are the vertical components of the conductivity and permittivity, respectively.

For a one-dimensional (1-D) formation, the only parameter that must be considered is the dipping angle. Figure 1.4 shows the triaxial induction tool in a 1-D multi-layered transversely isotropic formation.

1.1.4 Computation Time

The software is fast because an analytical solution is used. The computation time mainly depends on the number of layers and receiver points. For the five-layer model in Figure 1.5, this simulation method costs 9.15625 seconds for 184 receiver points on an Intel 2.4GHz (core) PC.

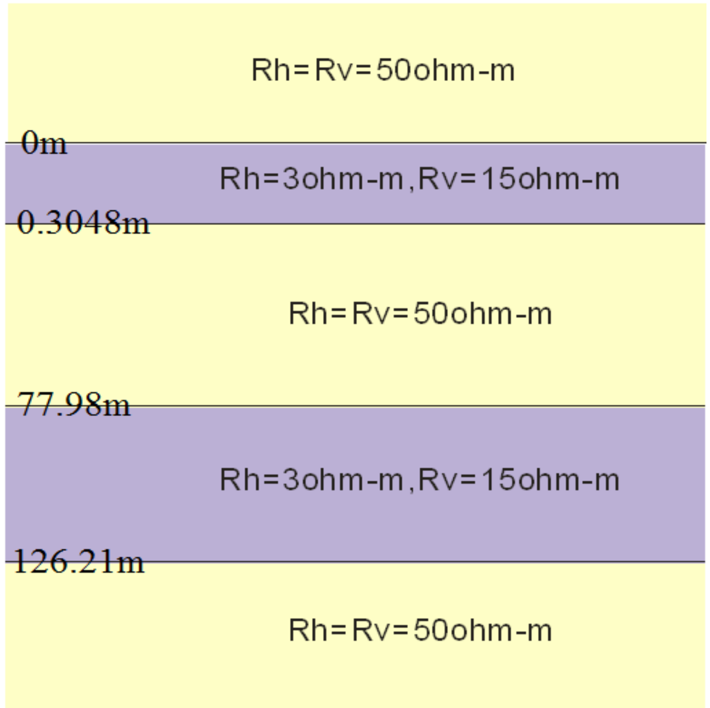

Figure 1.5. 5-layer formation structure.

1.1.5 Objective

The simulation method that is used to forward modeling the response of triaxial induction tools in a 1-D multi-layered transverse isotropic formation can function properly at low frequency. However, given that the frequency of dielectric tools' is higher than that of triaxial induction tools, the frequency limitation for this simulation method should be explored to make sure it can function properly.

In this thesis, we mainly focus on using triaxial induction and dielectric tools at different frequencies. The results of the triaxial induction tools at frequencies lower than 200 kHz were checked by previous works. This simulation method can obtain fast and accurate results. Thus, frequencies higher than the aforementioned should be checked.

The fast Hankel transform can satisfy speed requirements and has the accuracy that the tool requires. To calculate the reflection and transmission coefficients, a fast algorithm for the computation of triaxial induction logging tools in a layered transverse isotropic formation is used. Based on the electromagnetic (EM) field in planarly layered media, formulations of the EM fields generated by three transmitting coils are derived. Compared with the algorithm using the coefficient propagator method previously developed, the proposed algorithm calculates the reflection and transmission coefficients only once for each layer regardless of the position of the transmitters and, therefore, significantly speeds up the computation.

Specifically, this thesis aims to complete the following tasks:

1. Study magnetic field components in a homogeneous transverse isotropic medium, and derive all nine components of the magnetic field generated by a magnetic dipole in a homogeneous transverse isotropic medium.

2. Study the magnetic field response of a triaxial induction tool in a 1-D multiple layered transverse isotropic formation, and obtain nine components of the magnetic field generated by a magnetic dipole in a 1-D multiple layered transverse isotropic formation.

3. Try frequencies from 10 MHz to 50 MHz for triaxial induction tools with one transmitting coil and one receiving coil, and then analyze the results to determine if this simulation method can handle those frequencies.

4) Try frequencies that range from 300 MHz to 1 GHz for dielectric tools with one transmitting coils and two receiving coils, then analyze the results.

Chapter 2 Formulation

The transmitting and receiving coils are assumed to be sufficiently small and replaced by point magnetic dipoles in the modeling. The magnetic source excitation of the triaxial tool can be expressed as

$$\boldsymbol{M} = (M_x, M_y, M_z)\delta(\boldsymbol{r}). \tag{3}$$

2.1 Magnetic Field Components in a Homogeneous Transverse Isotropic Medium

The following are Maxwell's equations for the electric and magnetic fields:

$$\nabla \times \boldsymbol{H}(\boldsymbol{r}) = (\boldsymbol{\sigma} - i\omega\boldsymbol{\varepsilon})\boldsymbol{E}(\boldsymbol{r}) = \boldsymbol{\sigma}'\boldsymbol{E} \tag{4}$$

and

$$\nabla \times \boldsymbol{E}(\boldsymbol{r}) = i\omega\mu \boldsymbol{H}(\boldsymbol{r}) + i\omega\mu \boldsymbol{M}_s(\tag{5}$$

For convenience, a complex conductivity tensor is defined as follows:

$$\boldsymbol{\sigma}' = \begin{bmatrix} \sigma_h' & 0 & 0 \\ 0 & \sigma_h' & 0 \\ 0 & 0 & \sigma_v' \end{bmatrix} = \begin{bmatrix} \sigma_h - i\omega\varepsilon_h & 0 & 0 \\ 0 & \sigma_h - i\omega\varepsilon_h & 0 \\ 0 & 0 & \sigma_v - i\omega\varepsilon_v \end{bmatrix}. \tag{6}$$

The Hertz vector is potential $\boldsymbol{\pi}$–and scalar potentialΦ. By substituting Equations (4) and (5), the following can be obtained:

$$\boldsymbol{\sigma}' \cdot \boldsymbol{E}(\boldsymbol{r}) = i\omega\mu\sigma_h'\nabla \times \boldsymbol{\pi} \tag{7}$$

and

$$\boldsymbol{H}(\boldsymbol{r}) = i\omega\mu\sigma_h{}'\boldsymbol{\pi} + \nabla\Phi. \tag{8}$$

A gauge condition is then used for the scalar potential:

$$\nabla\cdot(\boldsymbol{\sigma}'\cdot\pi) = \sigma_v{}'\Phi. \tag{9}$$

By substituting Equation (9) into Equations (7) and (8), the following can be obtained:

$$\boldsymbol{E}(\boldsymbol{r}) = i\omega\mu\sigma_h{}'\boldsymbol{\sigma}'^{-1}\cdot\nabla\times\boldsymbol{\pi} \tag{10}$$

and

$$\boldsymbol{H}(\boldsymbol{r}) = i\omega\mu\sigma_h{}'\boldsymbol{\pi} + \nabla\left(\frac{\nabla\cdot(\boldsymbol{\sigma}'\cdot\boldsymbol{\pi})}{\sigma_v{}'}\right). \tag{11}$$

The derivation of the Hertz vector potential in a multiple layer formation is shown in Appendix I.

For an x-directed magnetic dipole $\boldsymbol{M} = (M_x, 0, 0)^T$, the Hertz vector potential is given by

$$\boldsymbol{\pi} = \pi_x\hat{x} + \pi_z\hat{z}, \tag{12}$$

where

$$\pi_x = \frac{M_x}{4\pi\lambda}\frac{e^{ik_v s}}{s} \tag{13}$$

and

$$\pi_z = \frac{M_x x}{4\pi\rho^2}\left(\lambda z\frac{e^{ik_v s}}{s} - z\frac{e^{ik_h r}}{r}\right), \tag{14}$$

where

$$\lambda^2 = \sigma_h' / \sigma_v', \tag{15}$$

$$k_h^2 = i\omega\mu\sigma_h', \tag{16}$$

$$k_v^2 = i\omega\mu\sigma_v', \tag{17}$$

$$r = \sqrt{x^2 + y^2 + z^2}, \tag{18}$$

$$\rho = \sqrt{x^2 + y^2} \tag{19}$$

and

$$s = \sqrt{x^2 + y^2 + \lambda^2 z^2}. \tag{20}$$

For a y-directed magnetic dipole $\boldsymbol{M} = (0, M_y, 0)^T$, the Hertz vector potential is given by

$$\pi = \pi_y \hat{y} + \pi_z \hat{z}, \tag{21}$$

where

$$\pi_y = \frac{M_y}{4\pi\lambda} \frac{e^{ik_v s}}{s} \tag{22}$$

and

$$\pi_z = \frac{M_y y}{4\pi\rho^2} \left(\lambda z \frac{e^{ik_v s}}{s} - z \frac{e^{ik_h r}}{r} \right). \tag{23}$$

For a z-directed magnetic dipole $\boldsymbol{M} = (0, 0, M_z)^T$, the Hertz vector potential only has a z component:

$$\boldsymbol{\pi} = \pi_z \hat{z}, \tag{24}$$

where

$$\pi_z = \frac{M_z}{4\pi} \frac{e^{ik_h r}}{r}. \tag{25}$$

By substituting (12)–(25) into (11), all the nine components of the magnetic field generated by a magnetic dipole in a homogeneous transverse isotropic medium can be obtained:

$$\begin{aligned} H_{xx} = {} & \frac{e^{ik_v s}}{4\pi}\left[\frac{k_h^2}{\lambda s} + \frac{ik_h s - k_h k_v x^2}{s\rho^2} - \frac{2ik_h x^2}{\rho^4}\right] - \\ & \frac{e^{ik_h r}}{4\pi}\left[\frac{ik_h r - k_h^2 x^2}{r\rho^2} - \frac{2ik_h x^2}{\rho^4} - \frac{ik_h}{r^2} + \frac{\left(k_h^2 x^2 + 1\right)}{r^3} + \frac{3ik_h x^2}{r^4} - \frac{3x^2}{r^5}\right], \end{aligned} \tag{26}$$

$$H_{yx} = H_{xy} = xy\frac{e^{ik_v s}}{4\pi\rho^2}\left[-\frac{k_h k_v}{s} - \frac{2ik_h}{\rho^2}\right] - \frac{e^{ik_h r} xy}{4\pi}\left[-\frac{k_h^2}{r\rho^2} - \frac{2ik_h}{\rho^4} + \frac{k_h^2}{r^3} + \frac{3ik_h}{r^4} - \frac{3}{r^5}\right], \tag{27}$$

$$H_{zx} = H_{xz} = -xz\frac{e^{ik_h r}}{4\pi r^3}\left[k_h^2 + \frac{3ik_h}{r} - \frac{3}{r^2}\right], \tag{28}$$

$$\begin{aligned} H_{yy} = {} & \frac{e^{ik_v s}}{4\pi}\left[\frac{k_h^2}{\lambda s} + \frac{ik_h s - k_h k_v y^2}{s\rho^2} - \frac{2ik_h y^2}{\rho^4}\right] \\ & - \frac{e^{ik_h r}}{4\pi}\left[\frac{ik_h r - k_h^2 y^2}{r\rho^2} - \frac{2ik_h y^2}{\rho^4} - \frac{ik_h}{r^2} + \frac{\left(k_h^2 y^2 + 1\right)}{r^3} + \frac{3ik_h y^2}{r^4} - \frac{3y^2}{r^5}\right], \end{aligned} \tag{29}$$

$$H_{zy} = H_{yz} = -yz\frac{e^{ik_h r}}{4\pi r^3}\left[k_h^2 + \frac{3ik_h}{r} - \frac{3}{r^2}\right] \tag{30}$$

and

$$H_{zz} = \frac{e^{ik_h r}}{4\pi r}\left[k_h^2 + \frac{ik_h}{r} - \frac{\left(k_h^2 z^2 + 1\right)}{r^2} - \frac{3ik_h z^2}{r^3} + \frac{3z^2}{r^4}\right]. \tag{31}$$

2.2 Magnetic Field Response of a Triaxial Induction Tool in a 1-D Multiple Layered Transverse Isotropic Formation

For a general case, the magnetic field response of a triaxial induction tool in a 1-D multi-layered transverse isotropic formation is considered.

2.2.1 A *z*-directed Magnetic Dipole in a Multi-layered Transverse Isotropic Formation

The vector potential only has a *z* component:

$$\boldsymbol{\pi} = \pi_z \hat{z}. \tag{32}$$

Within the ith layer of the formation ($z_{i\text{-}1} < z < z_i$), the vector potential is found to be as

$$\pi_{zi} = \frac{M_z}{4\pi}\int_0^{\infty}\left(\frac{\beta_i}{\xi_{hi}}e^{-\xi_{hi}|z-z_0|} + F_i e^{-\xi_{hi}z} + G_i e^{\xi_{hi}z}\right)\alpha J_0(\alpha\rho)d\alpha. \tag{33}$$

Substituting (32) into (11), the following is obtained:

$$\boldsymbol{H}_i = \frac{\partial^2\pi_{zi}}{\partial x\partial z}\hat{x} + \frac{\partial^2\pi_{zi}}{\partial y\partial z}\hat{y} + (i\omega\mu_0\sigma_h\pi_{zi} + \frac{\partial^2\pi_{zi}}{\partial z^2})\hat{z}. \tag{34}$$

The expressions for H_{xzi}, H_{yzi} and $H_{zzi}$are given by

$$H_{xzi} = \frac{M_z}{4\pi}\cos\phi\int_0^{\infty}\xi_{hi}\left(\frac{\beta_i}{\xi_{hi}}\frac{|z-z_0|}{z-z_0}e^{-\xi_{hi}|z-z_0|} + F_i e^{-\xi_{hi}z} - G_i e^{\xi_{hi}z}\right)\alpha^2 J_1(\alpha\rho)d\alpha, \tag{35}$$

$$H_{yzi} = \frac{M_z}{4\pi}\sin\phi\int_0^{\infty}\xi_{hi}\left(\frac{\beta_i}{\xi_{hi}}\frac{|z-z_0|}{z-z_0}e^{-\xi_{hi}|z-z_0|} + F_i e^{-\xi_{hi}z} - G_i e^{\xi_{hi}z}\right)\alpha^2 J_1(\alpha\rho)d\alpha \tag{36}$$

and

$$H_{zzi} = \frac{M_z}{4\pi} \int_0^\infty \left(\frac{\beta_i}{\xi_{hi}} e^{-\xi_{hi}|z-z_0|} + F_i e^{-\xi_{hi} z} + G_i e^{\xi_{hi} z} \right) \alpha^3 J_0(\alpha\rho) d\alpha, \tag{37}$$

where

$$\xi_{hi} = \left(\alpha^2 - k_{hi}^2\right)^{1/2},\ \beta_i = \begin{cases} 0, \text{ if } M_z \text{ is not in the ith layer} \\ 1, \text{ if } M_z \text{ is in the ith layer.} \end{cases} \tag{38}$$

In Equations (35) through (37), $J_0(\alpha\rho)$ is the 0-th order Bessel function. The symbol ρ implies that the equivalent transmitter and receiver in a formation coordinate are not coaxial but should be parallel. The symbol F_i is the magnitude of the reflection magnetic fields and G_i is the magnitude of the refraction magnetic fields.

Boundary conditions are used to calculate F_i and G_i. The equations are

$$\frac{\partial \pi_{zi}}{\partial z} = \frac{\partial \pi_{z(i+1)}}{\partial z} \tag{39}$$

and

$$\mu_i \pi_{zi} = \mu_{i+1} \pi_{z(i+1)}. \tag{40}$$

2.2.2 An *x*-directed Magnetic Dipole in Multi-layered Transverse Isotropic Media

An *x*-directed magnetic dipole generated vector potential in both *x* and *z* direction,

$$\boldsymbol{\pi} = \pi_x \hat{x} + \pi_z \hat{z}, \tag{41}$$

where the ith layer of the formation ($z_{i\text{-}1} < z < z_i$), the components of the vector potential are given by

$$\pi_{xi} = \frac{M_x}{4\pi\lambda_i}\int_0^\infty \left(\frac{\beta_i}{\xi_{vi}} e^{-\xi_{vi}\lambda_i|z-z_0|} + P_i e^{-\xi_{vi}\lambda_i z} + Q_i e^{\xi_{vi}\lambda_i z} \right) \alpha J_0(\alpha\rho) d\alpha \tag{42}$$

and

$$\begin{aligned} \pi_{zi} &= \frac{M_x}{4\pi}\cos\phi \int_0^\infty \left(S_i e^{-\xi_{hi} z} + T_i e^{\xi_{hi} z} - \xi_{vi} P_i e^{-\xi_{vi}\lambda_i z} + \xi_{vi} Q_i e^{\xi_{vi}\lambda_i z} \right) J_1(\alpha\rho) d\alpha \\ &+ \frac{M_x}{4\pi}\cos\phi \int_0^\infty \beta_i \left(e^{-\xi_{hi}|z-z_0|} - e^{-\xi_{vi}\lambda_i|z-z_0|} \right) \frac{|z-z_0|}{z-z_0} J_1(\alpha\rho) d\alpha. \end{aligned} \tag{43}$$

Substituting (41)-(43) into (11), the magnetic fields are obtained:

$$\begin{aligned} \boldsymbol{H}_i &= (i\omega\mu_0\sigma_h\pi_{xi} + \lambda_i^2 \frac{\partial^2\pi_{xi}}{\partial x^2} + \frac{\partial^2\pi_{zi}}{\partial x\partial z})\hat{x} + (\lambda_i^2 \frac{\partial^2\pi_{xi}}{\partial x\partial y} + \frac{\partial^2\pi_{zi}}{\partial y\partial z})\hat{y} \\ &+ (i\omega\mu_0\sigma_h\pi_{zi} + \lambda_i^2 \frac{\partial^2\pi_{xi}}{\partial x\partial z} + \frac{\partial^2\pi_{zi}}{\partial z^2})\hat{z}. \end{aligned} \tag{44}$$

The expression for the magnetic field components can then be obtained as:

$$\begin{aligned} H_{xxi} &= \frac{M_x}{4\pi}\int_0^\infty \begin{pmatrix} \frac{\beta_i}{\lambda_i\xi_{vi}} k_{hi}^2 \sin^2\phi e^{-\xi_{vi}\lambda_i|z-z_0|} - \beta_i \cos^2\phi \xi_{hi} e^{-\xi_{hi}|z-z_0|} \\ + \frac{P_i}{\lambda_i} k_{hi}^2 \sin^2\phi e^{-\xi_{vi}\lambda_i z} + \frac{Q_i}{\lambda_i} k_{hi}^2 \sin^2\phi e^{\xi_{vi}\lambda_i z} \\ -S_i \cos^2\phi \xi_{hi} e^{-\xi_{hi} z} + T_i \cos^2\phi \xi_{hi} e^{\xi_{hi} z} \end{pmatrix} \alpha J_0(\alpha\rho) d\alpha \\ &+ \frac{M_x}{4\pi\rho}\cos 2\phi \int_0^\infty \begin{pmatrix} \lambda_i \frac{\beta_i}{\xi_{vi}} k_{vi}^2 e^{-\xi_{vi}\lambda_i|z-z_0|} + \beta_i \xi_{hi} e^{-\xi_{hi}|z-z_0|} \\ +P_i\lambda_i k_{vi}^2 e^{-\xi_{vi}\lambda_i z} + Q_i\lambda_i k_{vi}^2 e^{\xi_{vi}\lambda_i z} \\ +S_i\xi_{hi} e^{-\xi_{hi} z} - T_i\xi_{hi} e^{\xi_{hi} z} \end{pmatrix} J_1(\alpha\rho) d\alpha, \end{aligned} \tag{45}$$

$$H_{yxi} = \frac{M_x}{4\pi}\sin\phi\cos\phi\int_0^\infty \begin{pmatrix} -\frac{\beta_i}{\lambda_i\xi_{vi}}k_{hi}^2 e^{-\xi_{vi}\lambda_i|z-z_0|} - \beta_i\xi_{hi}e^{-\xi_{hi}|z-z_0|} \\ -\frac{P_i}{\lambda_i}k_{hi}^2 e^{-\xi_{vi}\lambda_i z} - \frac{Q_i}{\lambda_i}k_{hi}^2 e^{\xi_{vi}\lambda_i z} \\ -S_i\xi_{hi}e^{-\xi_{hi}z} + T_i\xi_{hi}e^{\xi_{hi}z} \end{pmatrix} \alpha J_0(\alpha\rho)d\alpha$$

$$+\frac{M_x}{4\pi\rho}\sin 2\phi\int_0^\infty \begin{pmatrix} \lambda_i\frac{\beta_i}{\xi_{vi}}k_{vi}^2 e^{-\xi_{vi}\lambda_i|z-z_0|} + \beta_i\xi_{hi}e^{-\xi_{hi}|z-z_0|} \\ +P_i\lambda_i k_{vi}^2 e^{-\xi_{vi}\lambda_i z} + Q_i\lambda_i k_{vi}^2 e^{\xi_{vi}\lambda_i z} \\ +S_i\xi_{hi}e^{-\xi_{hi}z} - T_i\xi_{hi}e^{\xi_{hi}z} \end{pmatrix} J_1(\alpha\rho)d\alpha, \tag{46}$$

$$H_{zxi} = \frac{M_x}{4\pi}\cos\phi\int_0^\infty \left(\beta_i\frac{|z-z_0|}{z-z_0}e^{-\xi_{hi}|z-z_0|} + S_i e^{-\xi_{hi}z} + T_i e^{\xi_{hi}z}\right)\alpha^2 J_1(\alpha\rho)d\alpha, \tag{47}$$

$$\mu_i\frac{\partial\pi_{xi}}{\partial z} = \mu_{i+1}\frac{\partial\pi_{x(i+1)}}{\partial z}, \tag{48}$$

$$\mu_i\pi_{zi} = \mu_{i+1}\pi_{z(i+1)}, \tag{49}$$

$$k_{hi}^2\pi_{xi} = k_{h(i+1)}^2\pi_{x(i+1)}, \tag{50}$$

$$\lambda_i^2\frac{\partial^2\pi_{xi}}{\partial x^2} + \frac{\partial^2\pi_{zi}}{\partial x\partial z} = \lambda_{i+1}^2\frac{\partial^2\pi_{x(i+1)}}{\partial x^2} + \frac{\partial^2\pi_{z(i+1)}}{\partial x\partial z}, \tag{51}$$

where

$$\xi_{hi} = \left(\alpha^2 - k_{hi}^2\right)^{1/2} \tag{52}$$

and

$$\xi_{vi} = \left(\alpha^2 - k_{vi}^2\right)^{1/2}. \tag{53}$$

In Equations (42)–(47), P_i and S_i are the magnitudes of the reflected magnetic fields and Q_i and T_i are the magnitudes of the refracted magnetic fields.

2.2.3 A *y*-directed Magnetic Dipole in Multi-layered Transverse Isotropic Media

A *y*-directed magnetic dipole in multi-layered transverse isotropic media generates a vector potential in both *y* and *z* directions:

$$\boldsymbol{\pi} = \pi_y \hat{y} + \pi_z \hat{z}. \tag{54}$$

Within the ith layer of the formation, the vector potential and the magnetic fields are found to be as

$$\pi_{yi} = \frac{M_y}{4\pi\lambda_i}\int_0^\infty \left(\frac{\beta_i}{\xi_{vi}} e^{-\xi_{vi}\lambda_i|z-z_0|} + P_i e^{-\xi_{vi}\lambda_i z} + Q_i e^{\xi_{vi}\lambda_i z} \right) \alpha J_0(\alpha\rho) d\alpha \tag{55}$$

and

$$\begin{aligned}\pi_{zi} &= \frac{M_y}{4\pi}\sin\phi \int_0^\infty \left(S_i e^{-\xi_{hi} z} + T_i e^{\xi_{hi} z} - \xi_{vi} P_i e^{-\xi_{vi}\lambda_i z} + \xi_{vi} Q_i e^{\xi_{vi}\lambda_i z} \right) J_1(\alpha\rho) d\alpha \\ &+ \frac{M_y}{4\pi}\sin\phi \int_0^\infty \beta_i \left(e^{-\xi_{hi}|z-z_0|} - e^{-\xi_{vi}\lambda_i|z-z_0|} \right) \frac{|z-z_0|}{z-z_0} J_1(\alpha\rho) d\alpha.\end{aligned} \tag{56}$$

Substituting (47) into (11), the following is obtained:

$$\begin{aligned}\boldsymbol{H}_i &= (\lambda_i^2 \frac{\partial^2 \pi_{yi}}{\partial x \partial y} + \frac{\partial^2 \pi_{zi}}{\partial x \partial z})\hat{x} + (i\omega\mu_0\sigma_h\pi_{yi} + \lambda_i^2 \frac{\partial^2 \pi_{yi}}{\partial y^2} + \frac{\partial^2 \pi_{zi}}{\partial y \partial z})\hat{y} \\ &+ (i\omega\mu_0\sigma_h\pi_{zi} + \lambda_i^2 \frac{\partial^2 \pi_{yi}}{\partial y \partial z} + \frac{\partial^2 \pi_{zi}}{\partial z^2})\hat{z}.\end{aligned} \tag{57}$$

The magnetic fields generated by a *y*-directed magnetic dipole are given by

$$H_{xyi} = \frac{M_y}{4\pi}\sin\phi\cos\phi\int_0^\infty \begin{pmatrix} -\frac{\beta_i}{\lambda_i\xi_{vi}}k_{hi}^2 e^{-\xi_{vi}\lambda_i|z-z_0|} - \beta_i\xi_{hi}e^{-\xi_{hi}|z-z_0|} \\ -\frac{P_i}{\lambda_i}k_{hi}^2 e^{-\xi_{vi}\lambda_i z} - \frac{Q_i}{\lambda_i}k_{hi}^2 e^{\xi_{vi}\lambda_i z} \\ -S_i\xi_{hi}e^{-\xi_{hi}z} + T_i\xi_{hi}e^{\xi_{hi}z} \end{pmatrix} \alpha J_0(\alpha\rho)d\alpha$$

$$+\frac{M_y}{4\pi\rho}\sin 2\phi\int_0^\infty \begin{pmatrix} \lambda_i\frac{\beta_i}{\xi_{vi}}k_{vi}^2 e^{-\xi_{vi}\lambda_i|z-z_0|} + \beta_i\xi_{hi}e^{-\xi_{hi}|z-z_0|} \\ +\frac{P_i}{\lambda_i}k_{hi}^2 e^{-\xi_{vi}\lambda_i z} + \frac{Q_i}{\lambda_i}k_{hi}^2 e^{\xi_{vi}\lambda_i z} \\ +S_i\xi_{hi}e^{-\xi_{hi}z} - T_i\xi_{hi}e^{\xi_{hi}z} \end{pmatrix} J_1(\alpha\rho)d\alpha, \tag{58}$$

$$H_{yyi} = \frac{M_y}{4\pi}\int_0^\infty \begin{pmatrix} \frac{\beta_i}{\lambda_i\xi_{vi}}k_{hi}^2\cos^2\phi e^{-\xi_{vi}\lambda_i|z-z_0|} - \beta_i\sin^2\phi\xi_{hi}e^{-\xi_{hi}|z-z_0|} \\ +\frac{P_i}{\lambda_i}k_{hi}^2\cos^2\phi e^{-\xi_{vi}\lambda_i z} + \frac{Q_i}{\lambda_i}k_{hi}^2\cos^2\phi e^{\xi_{vi}\lambda_i z} \\ -S_i\sin^2\phi\xi_{hi}e^{-\xi_{hi}z} + T_i\sin^2\phi\xi_{hi}e^{\xi_{hi}z} \end{pmatrix} \alpha J_0(\alpha\rho)d\alpha$$

$$+\frac{M_y}{4\pi\rho}\cos 2\phi\int_0^\infty \begin{pmatrix} -\lambda_i\frac{\beta_i}{\xi_{vi}}k_{vi}^2 e^{-\xi_{vi}\lambda_i|z-z_0|} - \beta_i\xi_{hi}e^{-\xi_{hi}|z-z_0|} \\ -P_i\lambda_i k_{vi}^2 e^{-\xi_{vi}\lambda_i z} - Q_i\lambda_i k_{vi}^2 e^{\xi_{vi}\lambda_i z} \\ -S_i\xi_{hi}e^{-\xi_{hi}z} + T_i\xi_{hi}e^{\xi_{hi}z} \end{pmatrix} J_1(\alpha\rho)d\alpha, \tag{59}$$

$$H_{zyi} = \frac{M_y}{4\pi}\sin\phi\int_0^\infty \left(\beta_i\frac{|z-z_0|}{z-z_0}e^{-\xi_{hi}|z-z_0|} + S_i e^{-\xi_{hi}z} + T_i e^{\xi_{hi}z}\right)\alpha^2 J_1(\alpha\rho)d\alpha, \tag{60}$$

$$\mu_i\frac{\partial\pi_{xi}}{\partial z} = \mu_{i+1}\frac{\partial\pi_{x(i+1)}}{\partial z}, \tag{61}$$

$$\mu_i\pi_{zi} = \mu_{i+1}\pi_{z(i+1)}, \tag{62}$$

$$k_{hi}^2\pi_{xi} = k_{h(i+1)}^2\pi_{x(i+1)}, \tag{63}$$

$$\lambda_i^2\frac{\partial^2\pi_{xi}}{\partial x^2} + \frac{\partial^2\pi_{zi}}{\partial x\partial z} = \lambda_{i+1}^2\frac{\partial^2\pi_{x(i+1)}}{\partial x^2} + \frac{\partial^2\pi_{z(i+1)}}{\partial x\partial z}, \tag{64}$$

where

$$\xi_{hi} = \left(\alpha^2 - k_{hi}^2\right)^{1/2} \tag{65}$$

and

$$\xi_{vi} = \left(\alpha^2 - k_{vi}^2\right)^{1/2}. \tag{66}$$

Similarly, for the x-directed dipole, in (55)–(60), P_i and S_i are the magnitudes of the reflected magnetic fields, and Q_i and T_i are the magnitudes of the refracted magnetic fields.

2.2.4 Magnitude of Reflection and Refraction Magnetic Fields

To calculate the unknown magnitude of the transmission and reflection coefficients, boundary conditions are used.

P_i, Q_i, S_i and T_i for x and y-directed dipoles are first identified. From the continuity of the EM fields at the horizontal boundary $z = z_i$, the boundary conditions of the Hertz potential are

$$\mu_i \frac{\partial \pi_{yi}}{\partial z} = \mu_{i+1} \frac{\partial \pi_{y(i+1)}}{\partial z}, \tag{67}$$

$$\mu_i \pi_{zi} = \mu_{i+1} \pi_{z(i+1)}, \tag{68}$$

$$\lambda_i^2 \frac{\partial^2 \pi_{yi}}{\partial y^2} + \frac{\partial^2 \pi_{zi}}{\partial y \partial z} = \lambda_{i+1}^2 \frac{\partial^2 \pi_{x(i+1)}}{\partial y^2} + \frac{\partial^2 \pi_{z(i+1)}}{\partial y \partial z}, \tag{69}$$

and

$$k_{hi}^2 \pi_{yi} = k_{h(i+1)}^2 \pi_{y(i+1)} . \tag{70}$$

From Equations (54)–(57), P_i, Q_i, S_i and T_i can be determined.

The next step is to calculate the coefficients F_i and G_i for the z directional dipole. From the continuity of the EM fields at the horizontal boundary $z = z_i$, the boundary conditions of the Hertz potential are

$$\frac{\partial \pi_{zi}}{\partial z} = \frac{\partial \pi_{z(i+1)}}{\partial z} \tag{71}$$

and

$$\mu_i \pi_{zi} = \mu_{i+1} \pi_{z(i+1)} . \tag{72}$$

The final expression for the coefficients F_i and G_i can be derived by applying boundary conditions.

2.3 Magnetic Field Response of Triaxial Tools in Arbitrary Orientation

In practice, the orientation of the transmitter and receiver coils will be arbitrary in regards to the principal axes of the conductivity tensor of the formation. Figure 2.1 shows schematically the bed coordinate system described by (x, y, z) and the sonde coordinate system described by (x', y', z'). In Figure 2.1, α, β ,and γ denote the dipping, azimuthal, and orientation angle, respectively. The angle α is the relative deviation of the instrument axis *z* regard to the *z*-axis of the conductivity tensor. The angle β is the angle between the projections of the instrument axis *z* on the surface of the *x*-*y* plane and the *x*-axis of the formation coordinate. The angle γ represents the rotation of the tool around the *z*-axis.

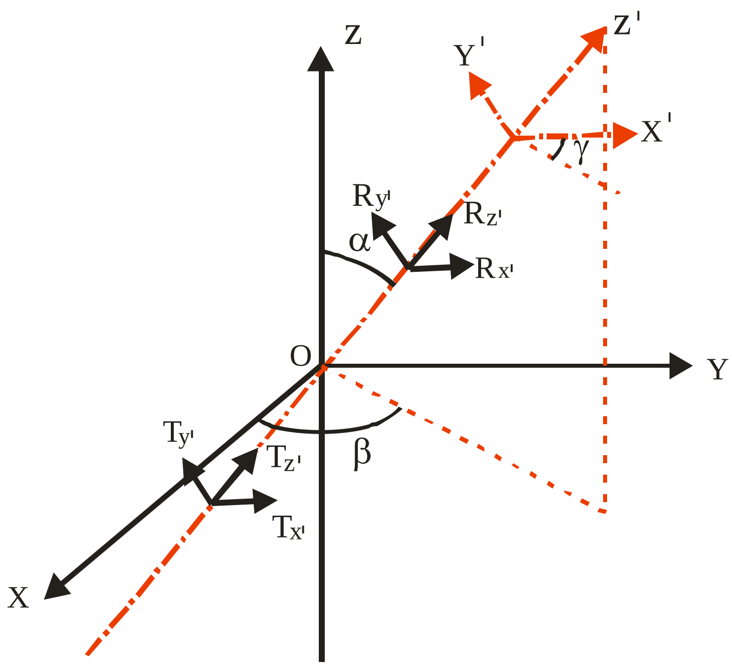

Figure 2.1, The bed coordinate system (*x*,*y*,*z*) and the sonde coordinate system (*x*', *y*', *z*').

The formation coordinate system can be related to the tool coordinate system by a rotation matrix **R** given by

$$\mathbf{R} = \begin{bmatrix} R_{11} & R_{12} & R_{13} \\ R_{21} & R_{22} & R_{23} \\ R_{31} & R_{32} & R_{33} \end{bmatrix} = \begin{bmatrix} \cos\alpha\cos\beta\cos\gamma - \sin\beta\sin\gamma & -\cos\alpha\cos\beta\sin\gamma - \sin\beta\cos\gamma & \sin\alpha\cos\beta \\ \cos\alpha\sin\beta\cos\gamma + \cos\beta\sin\gamma & -\cos\alpha\sin\beta\sin\gamma + \cos\beta\cos\gamma & \sin\alpha\sin\beta \\ -\sin\alpha\cos\gamma & \sin\alpha\sin\gamma & \cos\alpha \end{bmatrix}. \tag{73}$$

Consequently, the coupling between the magnetic field components and the magnetic dipoles in the tool system is given by

$$\boldsymbol{H}' = \mathbf{R}^{T}\boldsymbol{H}\mathbf{R}. \tag{74}$$

Equation (74) is then used to obtain the final magnetic fields.

Chapter 3 Dielectric Tool

3.1 Introduction

Dielectric measurement plays a vital role in distinguishing freshwater and carbonates. In nature, reservoir rocks are often sedimentary that comprise a grain and a cement rock matrix with interconnecting void spaces (pores). The formation of water, oil and gas is filled in pores. Resistivity logging is possible because formation rocks can transmit an electric current through the absorbed saline water contained inside their pores, but not through the insulating matrix of oil and gas. Water-bearing formations usually have a low electric resistivity compared with hydrocarbon-bearing formations. However, once the pores contain a high resistance of formation fluid such as fresh water, the resistivity logging tools fail to perform an accurate formation evaluation and provide incorrect formation property measurements.

Dielectric constant logging was developed to distinguish fresh water and oil, which was difficult to perform with resistivity logs alone. Dielectric tools are sensitive to detecting the formation with water that has an unknown salinity. Most recent dielectric tools use single frequencies around 1 GHz with one or two transmitters and one or two receivers. Array dielectric logging tools are widely used because of their multiple frequency channels. Array dielectric logging tools have various combinations of transmitter and receiver sets.

In this thesis, one transmitter and two receivers are used to simulate a dielectric tool, and different frequencies are employed to check the frequency limitation of the simulation. The transmitter and receivers are modeled as unit moment magnetic dipoles and compute the tool responses are computed.

3.2 Difference from a Triaxial Induction Tool

Dielectric tools use the same formulation as triaxial induction tools. However, a tool pad has one or more transmitters and two or more receivers. The working frequency of dielectric tools is higher than that of triaxial induction tools. In industry applications, triaxial induction tools use frequencies not higher than 100 MHz. Dielectric tools usually work at around 1 GHz. They have only two directions of transmitters and receivers. For triaxial induction tools, three directions of transmitters and receivers can obtain nine components of the magnetic field.

3.3 Dielectric Tool Response

Tool response is defined as the attenuation and phase difference between the received field from receivers for a tool with one transmitter and two receivers. Figure 3.1 shows the attenuation and phase difference.

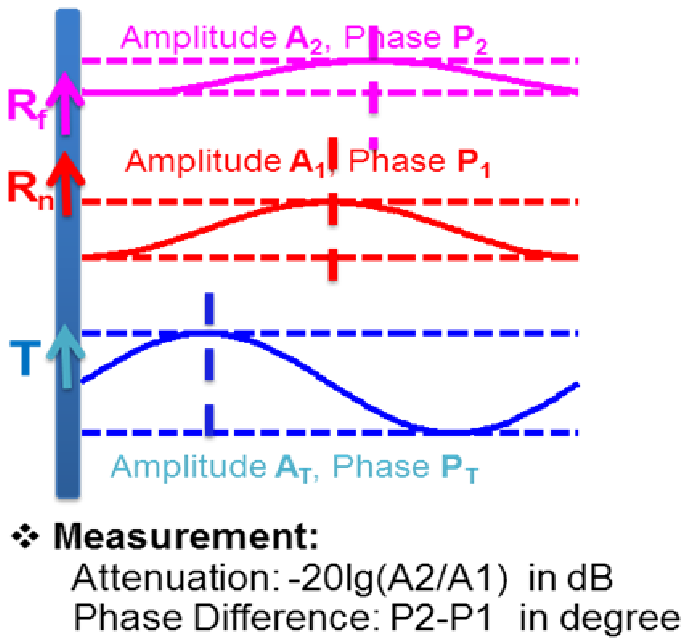

Figure 3.1. One-transmitter-two-receiver-antenna-array responses.

The amplitude and phase can be easily obtained for each receiver based on the magnetic field. The equations shown in Figure 3.1 are then used to calculate the attenuation and phase difference of the two receivers.

Chapter 4 will show that attenuation and phase difference can clearly demonstrate information for the formation.

Chapter 4 Simulation Results and Analysis

This chapter mainly focuses on the frequency of induction tools simulated in the algorithm. The simulation method used in this thesis is called TIRTI09, which is programmed in Fortran. A new version of this simulation method is called TIRTI10. However, the basic idea and functions are the same. The only difference is TIRTI10 can calculate magnetic fields faster using a different method for the calculation of transmission and reflection coefficients. But this does not influence the frequency limitation in the simulation of the induction tool.

4.1 Example I

A tool with one transmitting coil and one receiving coil is simulated at frequencies 10 MHz, 30 MHz and, 50 MHz. The spacing of the tool is set as 20 inches and 4 inches.

Figure 4.1 shows the formation used in this thesis. The formation has seven layers, and Table 1 shows the horizontal and vertical conductivities of each layer.

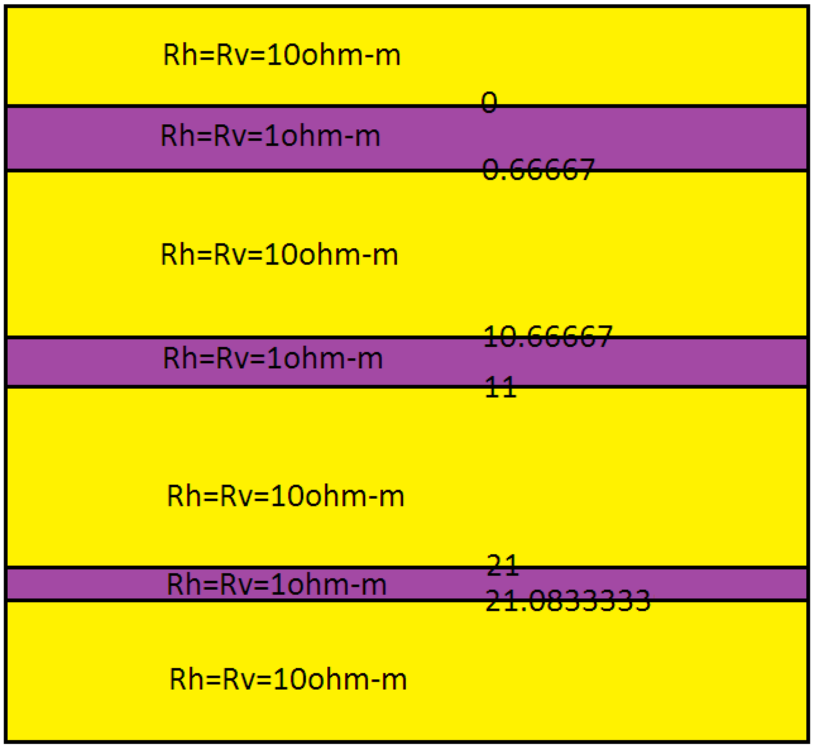

Figure 4.1. Formation layouts for a seven-layer transverse isotropic formation.

Table 4.1. Formation data for a seven-layer transverse isotropic formation.

Horizontal Conductivities (s/m)	Vertical Conductivities (s/m)	Depth (feet)
0.1	0.1	-10~0
1	1	0~0.666667
0.1	0.1	0.66667~10.666667
1	1	10.66667~11
0.1	0.1	11~21
1	1	21~21.0833333
0.1	0.1	21.0833333~31.0833333

The tool structure is shown in Figure 4.2.

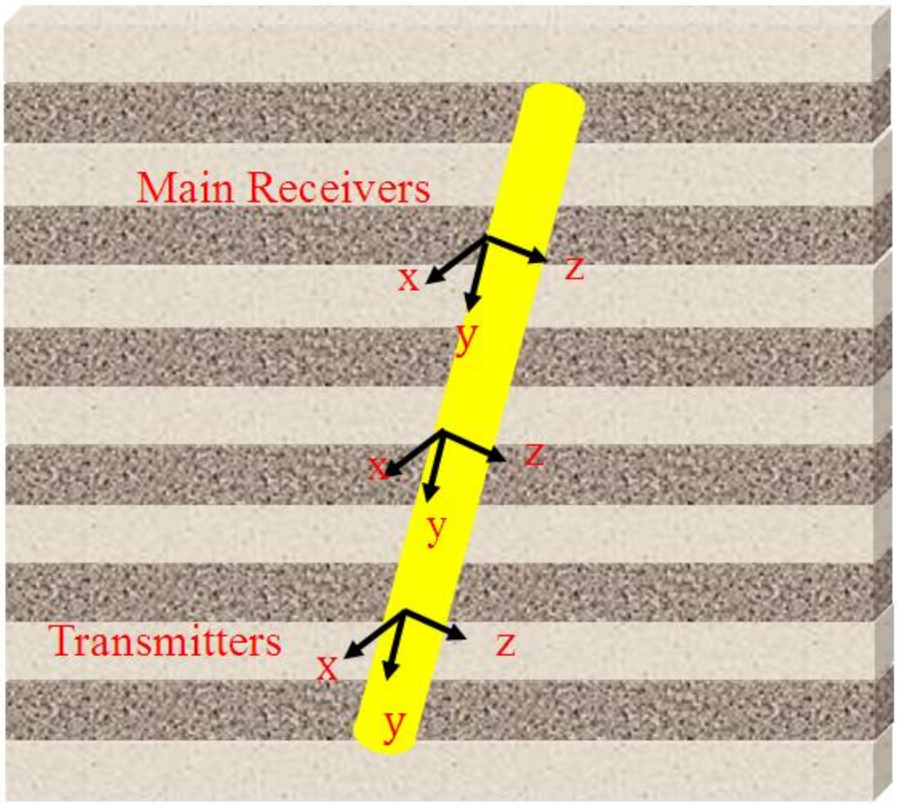

Figure 4.2. Tool structure for the simulation.

The tool has one transmitter coil and one receiver coil. The number of turns on the transmitter coil is one, and that of the receiver coil is also one. The dipping angle is 0 degrees, the azimuth angle is 0 degrees, and the rotation angle is 0 degrees. The relative permittivity is selected as 10.0 for each layer.

4.1.1 Frequency Results for the 20-inch Triaxial Induction Tool

In Figures 4.3 to 4.12, 10 MHz frequency results are plotted by a red solid line, 30 MHz frequency results by a green dotted line, and 50 MHz frequency results by a blue dotted line. These results do not show the exact position of each layer.

The formation used to simulate in this thesis has seven layers, and three thin layers can be deduced from the simulation results. However, given that the spacing of this tool is slightly large for these types of thin layers, the width difference between each layer cannot be identified. The width of each layer is the same, which can be determined from all the results obtained. In the next part the space will be decreased to check the results.

The imaginary parts of the results reflect the structure of the formation. We therefore mainly focus on the imaginary parts.

For all the results, we mainly focus on the *zz* component because our dipping angle is 0 degrees, and the *zz* component can clearly reflect the structure of the formation if the results are good.

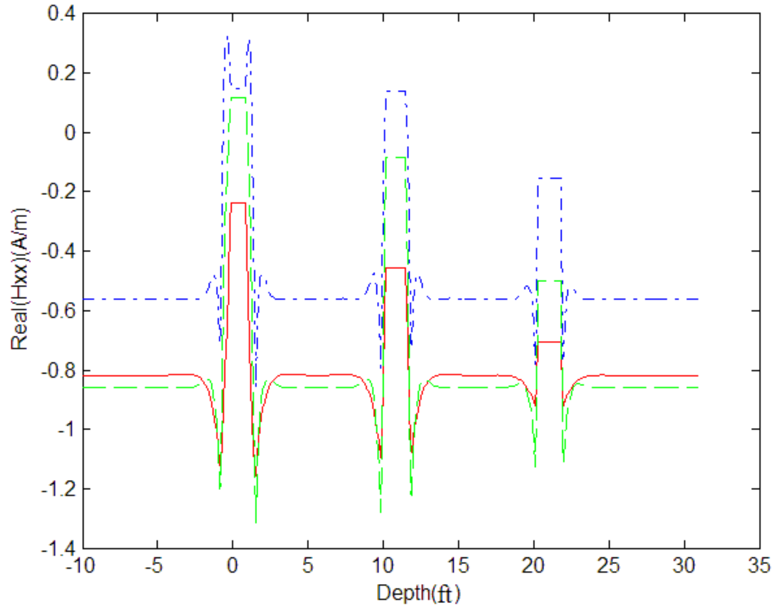

Figure 4.3. H_{xx} real part when frequencies are 10 MHz, 30 MHz, and 50 MHz, and the tool space is 20 inches.

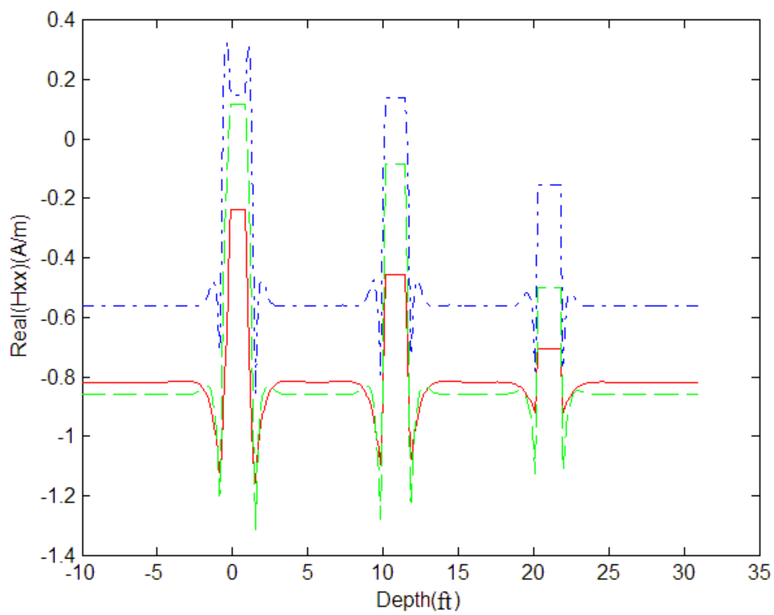

Figure 4.4. H_{xx} imaginary part when frequencies are 10 MHz, 30 MHz, and 50 MHz, and the tool space is 20 inches.

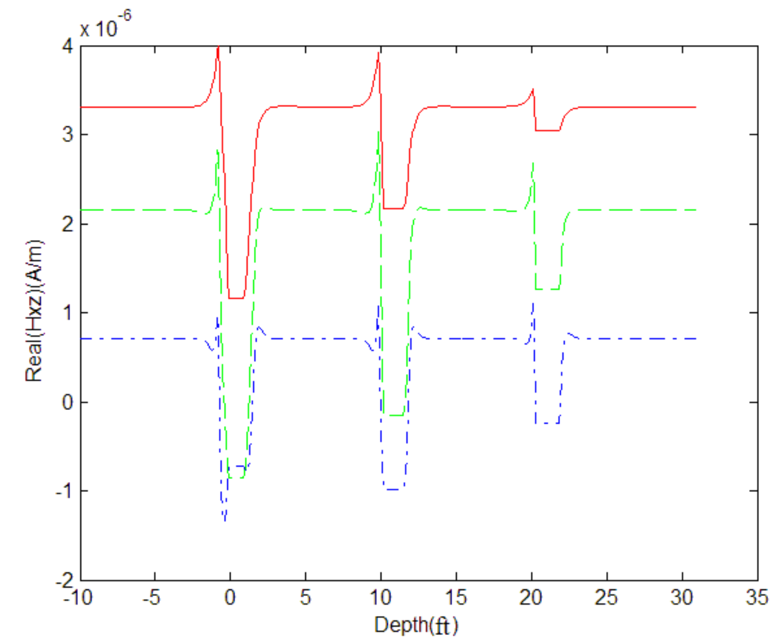

Figure 4.5. H_{xz} real part when frequencies are 10 MHz, 30 MHz, and 50 MHz, and the tool space is 20 inches.

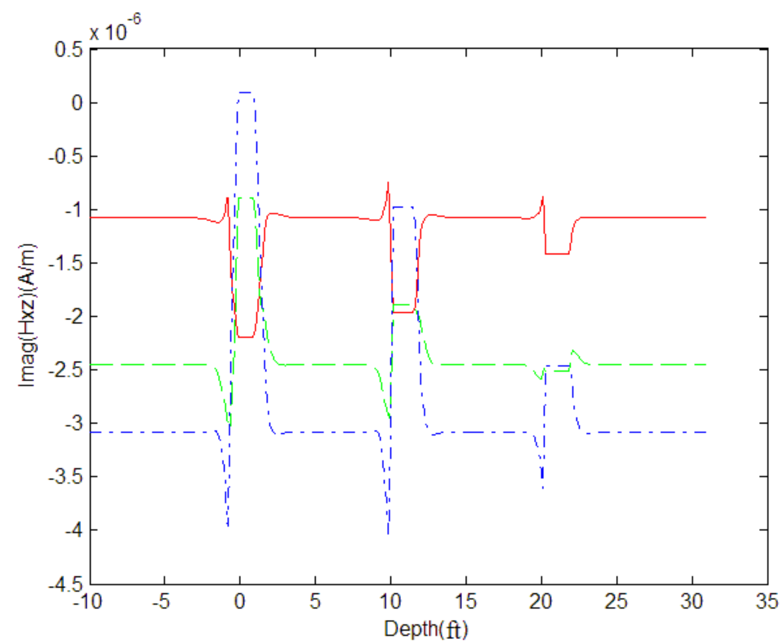

Figure 4.6. H_{xz} imaginary part when frequencies are 10MHz, 30MHz, and 50MHz, and the tool space is 20 inches.

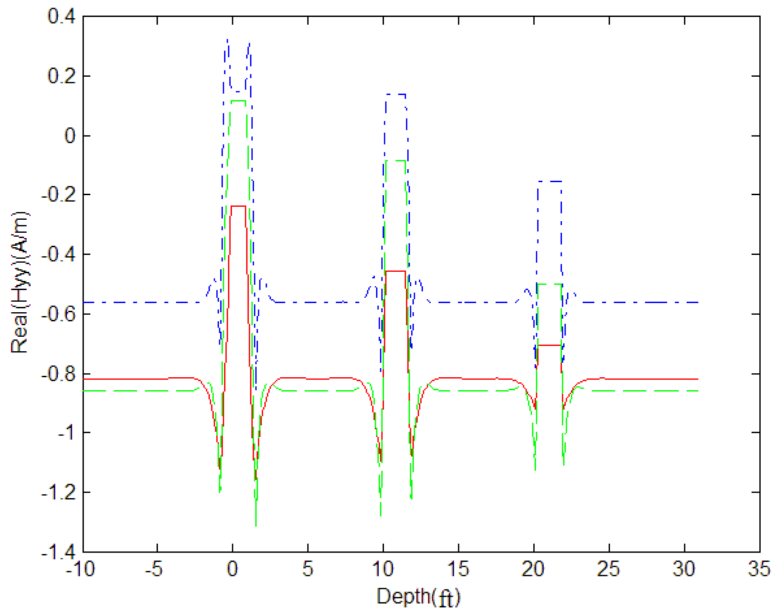

Figure 4.7. H_{yy} real part when frequencies are 10 MHz, 30 MHz, and 50 MHz, and the tool space is 20 inches.

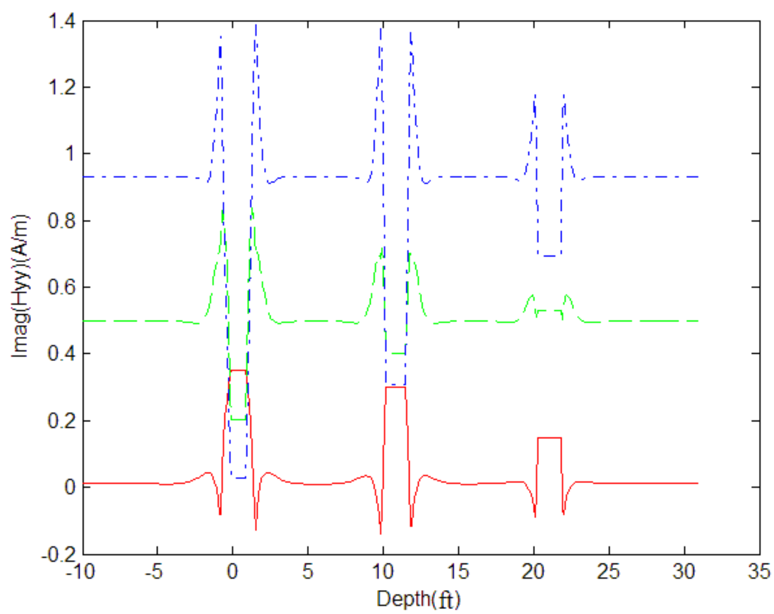

Figure 4.8. H_{yy} imaginary part when frequencies are 10 MHz, 30 MHz, and 50 MHz, and the tool space is 20 inches.

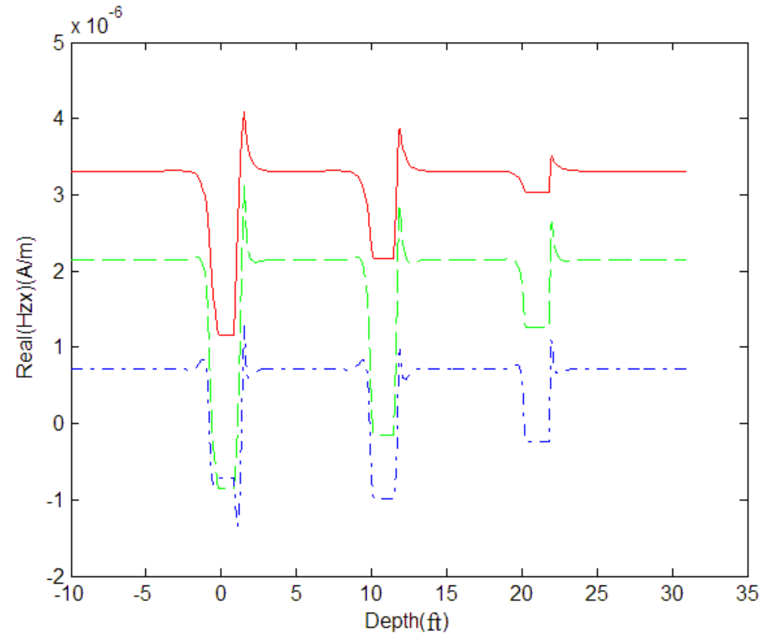

Figure 4.9. H_{zx} real part when frequencies are 10 MHz, 30 MHz, and 50 MHz, and the tool space is 20 inches.

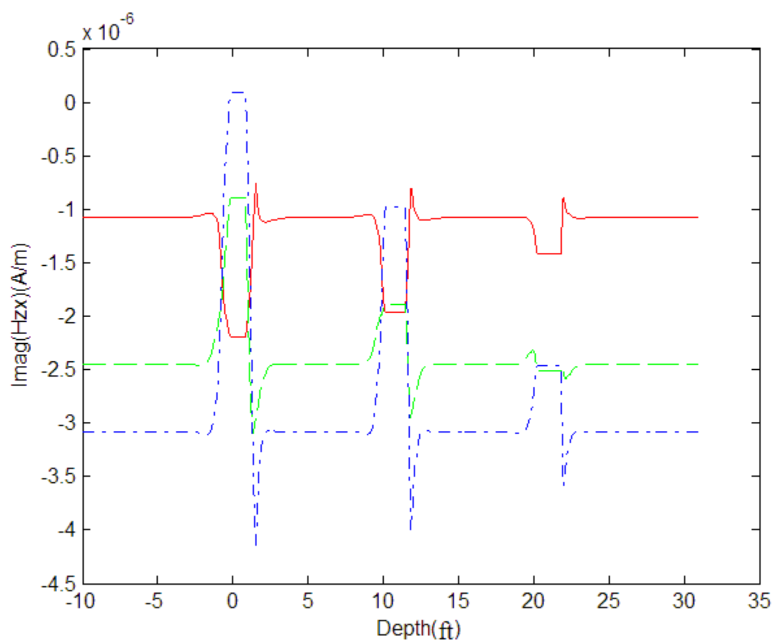

Figure 4.10. H_{zx} imaginary part when frequencies are10 MHz, 30 MHz, and 50 MHz, and the tool space is 20 inches.

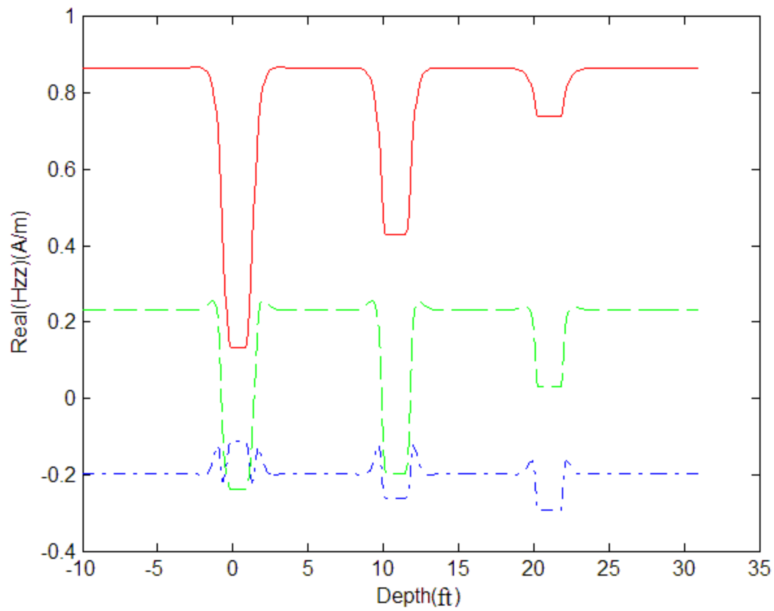

Figure 4.11. H_{zz} real part when frequencies are 10 MHz, 30 MHz, and 50 MHz, and the tool space is 20 inches.

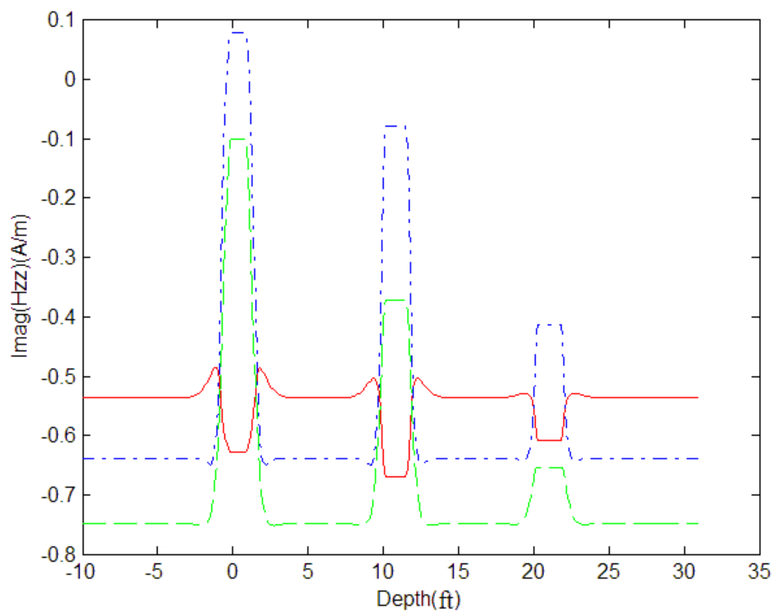

Figure 4.12. H_{zz} imaginary part when frequencies are 10 MHz, 30 MHz, and 50 MHz, and the tool space is 20 inches.

4.1.2 Frequency Results for the 4-inch Triaxial Induction Tool

In Figures 4.13 to 4.22, all results show with accuracy the position of the thin layers. Thus, for appropriate tool spacing, this simulation method can simulate the triaxial induction tool with accuracy.

We focus on the imaginary parts of the results and mainly on the *zz* component, which can clearly show the structure of the formation if the results are good.

The difference for each layer can be identified from these results. The width of the 8-inch layer is the largest. The 8-inch layer also has the highest amplitude in the three layers. The 1-inch layer has the smallest width and amplitude.

From 10 MHz to 50 MHz frequency, we can conclude that as frequency increases, the amplitude of each layer increases. However, the shape of each layer does not change as frequency increases.

For dielectric tools, we will check the frequency limitation to determine whether or not this simulation method can handle a frequency as high as 1 GHz. If this simulation method can obtain results higher than 1 GHz, we can use this simulation method to simulate dielectric tools. If not, we will obtain a frequency limitation of this simulation method for future research.

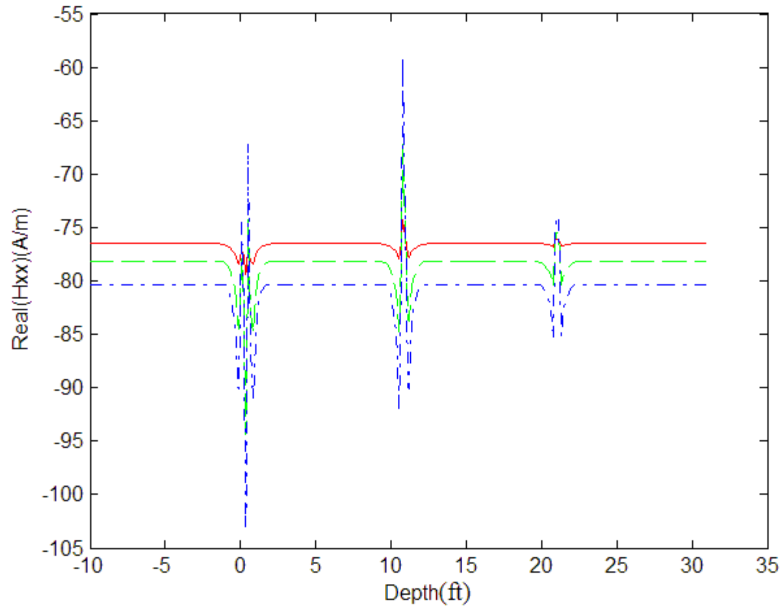

Figure 4.13. H_{xx} real part when frequencies are 10 MHz, 30 MHz, and 50 MHz, and the tool space is 4 inches.

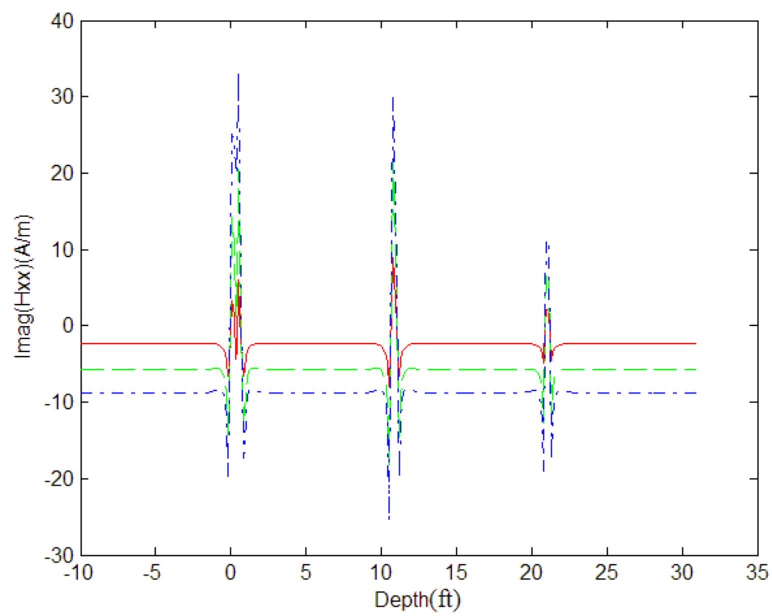

Figure 4.14. H_{xx} imaginary part when frequencies are 10 MHz, 30 MHz, and 50 MHz, and the tool space is 4 inches.

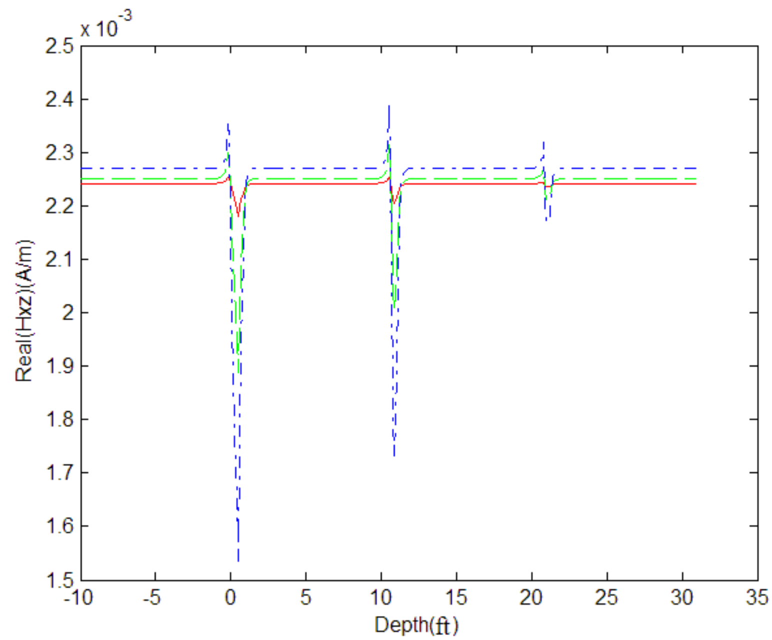

Figure 4.15. H_{xz} real part when frequencies are 10 MHz, 30 MHz, and 50 MHz, and the tool space is 4 inches.

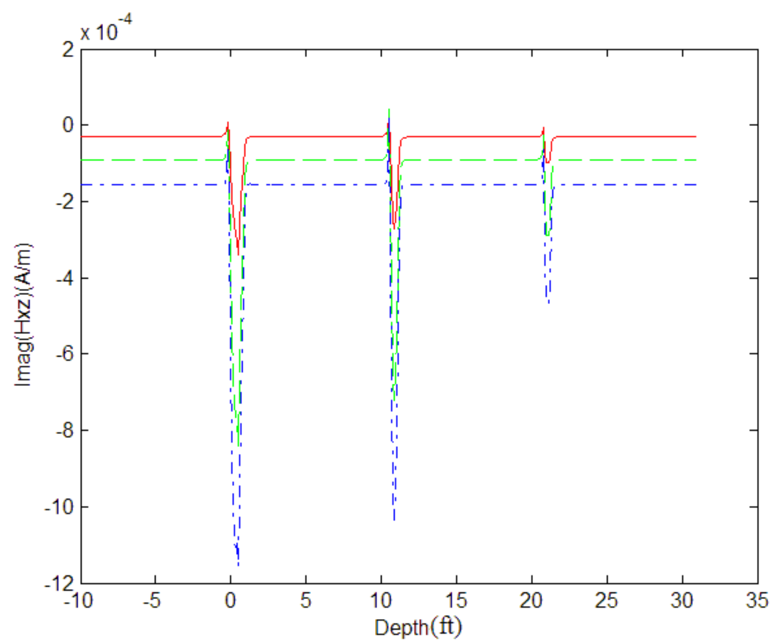

Figure 4.16. H_{xz} imaginary part when frequencies are 10 MHz, 30 MHz, and 50 MHz, and the tool space is 4 inches.

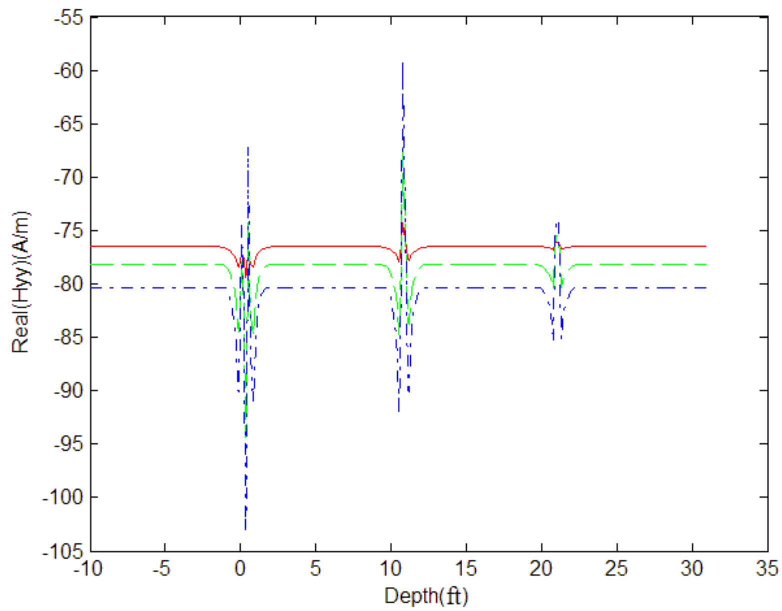

Figure 4.17. H_{yy} real part when frequencies are 10 MHz, 30 MHz, and 50 MHz, and the tool space is 4 inches.

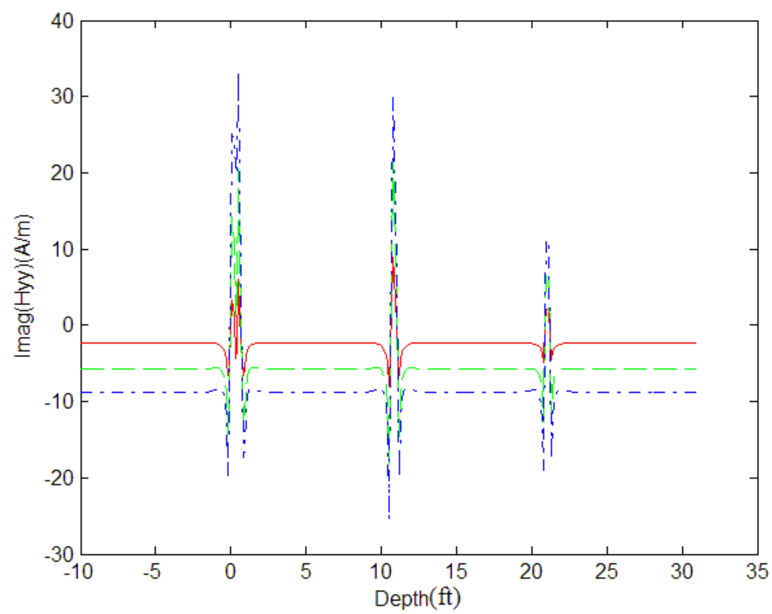

Figure 4.18. H_{yy} imaginary part when frequencies are 10 MHz, 30 MHz, and 50 MHz, and the tool space is 4 inches.

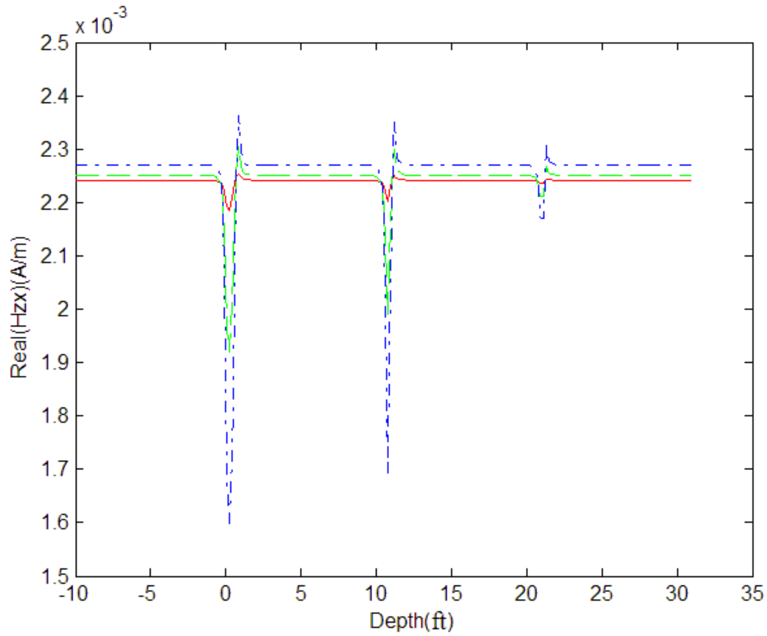

Figure 4.19. H_{zx} real part when frequencies are 10 MHz, 30 MHz, and 50 MHz, and the ool space is 4 inches.

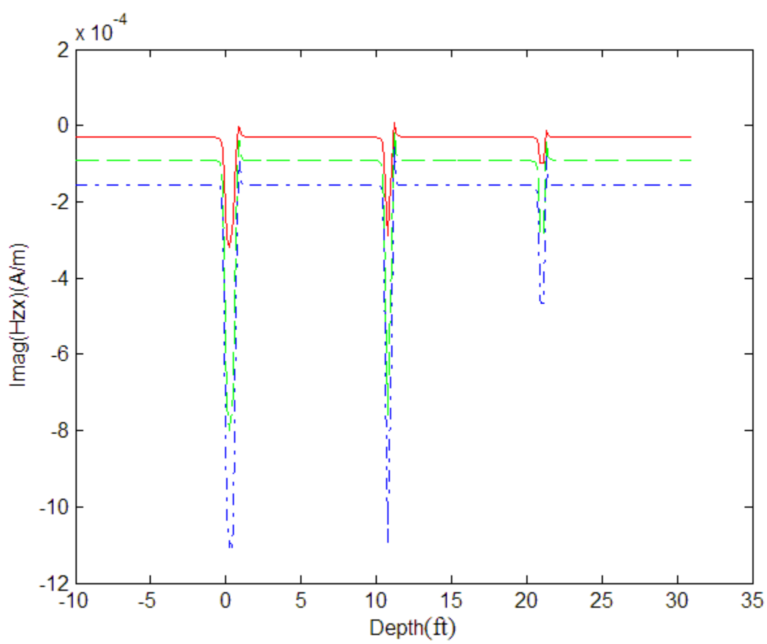

Figure 4.20. H_{zx} imaginary part when frequencies are 10 MHz, 30 MHz, and 50 MHz, and the tool space is 4 inches.

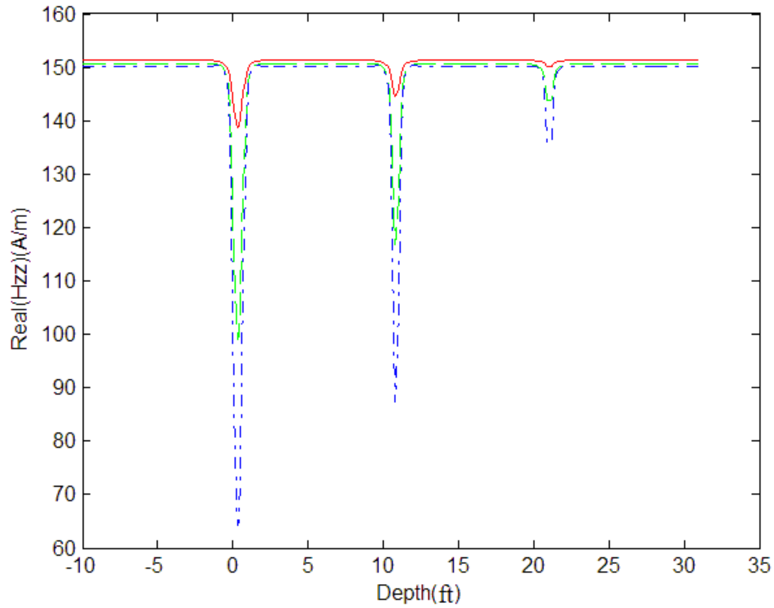

Figure 4.21. H_{zz} real part when frequencies are 10 MHz, 30 MHz, and 50 MHz, and the tool space is 4 inches.

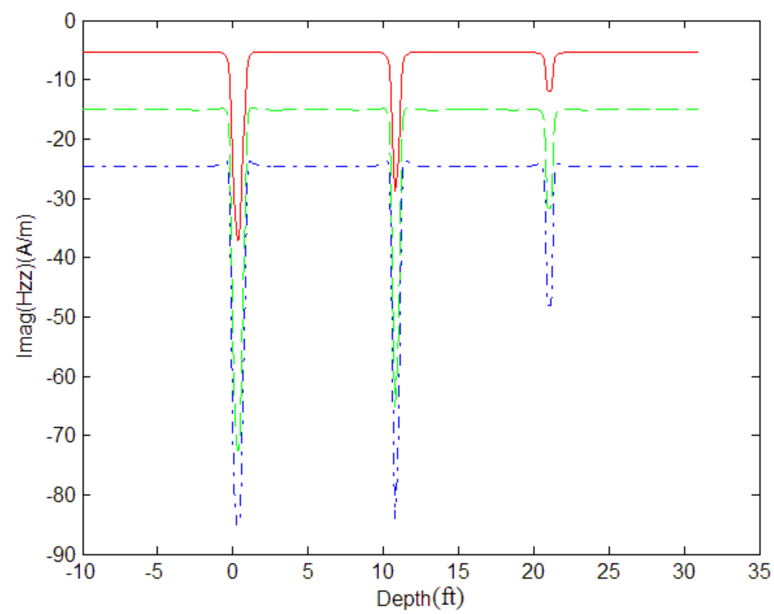

Figure 4.22. H_{zz} imaginary part when frequency is 10 MHz, 30 MHz and 50 MHz, the tool space is 4 inches.

4.2 Example II

In this example, a frequency from 300 MHz to 1 GHz is used to simulate the dielectric tool. The formation is the same as that in Example I.

Figure 4.23 shows the tool we use to simulate. The distance between transmitter T_1 and receiver R_1 is 6 inches and that between transmitter T_1 and receiver R_2 is 10 inches. Both the transmitter and receiver have only one coil for simplicity. Dielectric tools have *x* and *z*-direction components. Given that the dipping angle is zero, we mainly focus on the *zz* component, which can clearly show the structure of the formation if the results are good.

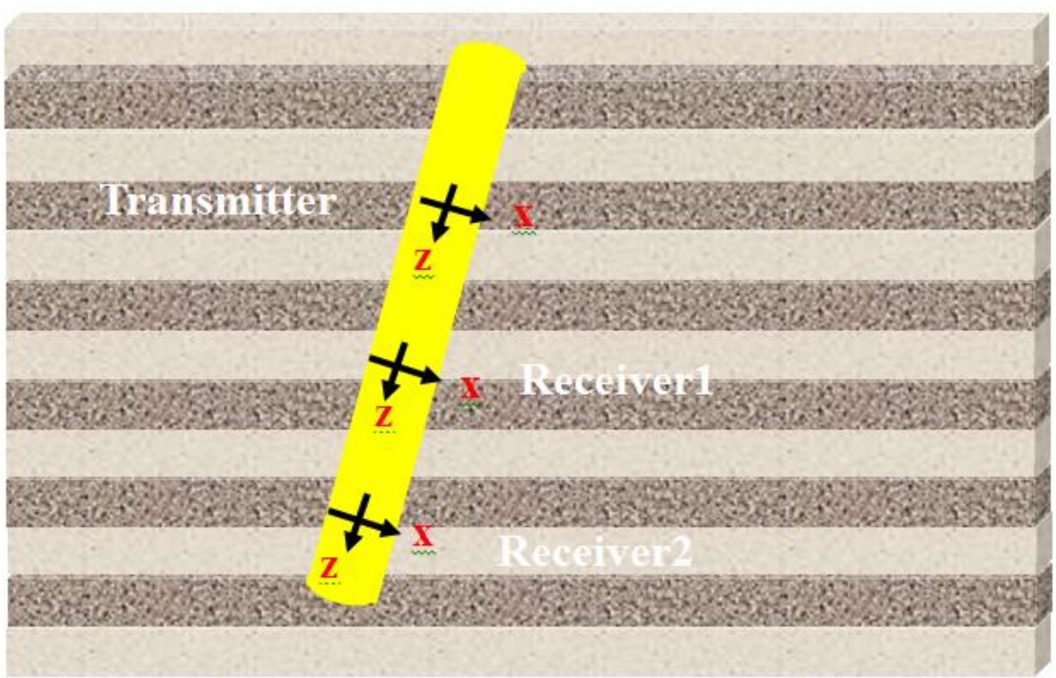

Figure 4.23. Structure of a dielectric tool.

4.2.1 300 MHz Frequency Results for the Dielectric Tool

Figures 4.24 and 4.25 show the attenuation of the *xx* and *zz* components for the 300 MHz frequency. Figures 4.26 and 4.27 show the phase shift of the *xx* and *zz* components for the 300 MHz frequency.

Considering that the layers are very thin, oscillations occur at the edge of each layer for attenuation and phase shift. For the layer with bigger width, the amplitude will also be bigger than for the others.

Based on the results, the 8-inch layer has the largest width and the 1-inch layer has the smallest width.

From these results, the information of the formation is illustrated. Three thin layers are identified.

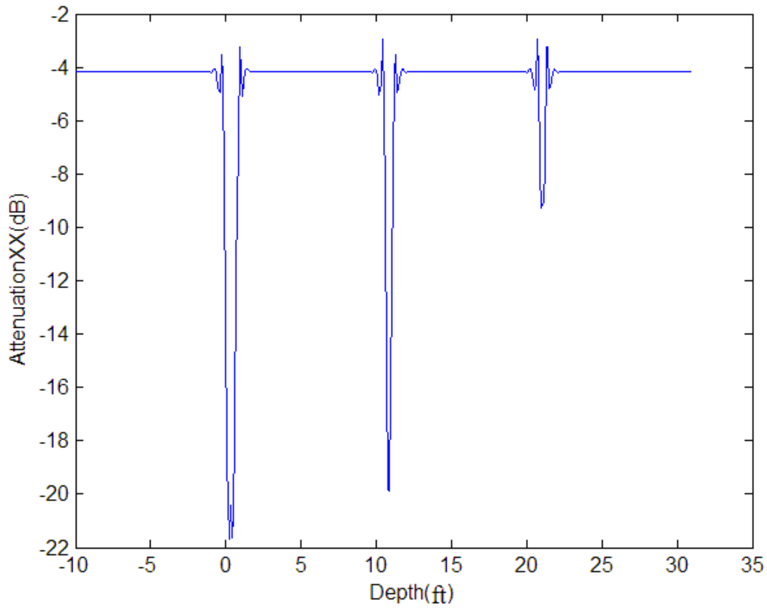

Figure 4.24. Attenuation of the *xx* component when frequency is 300 MHz.

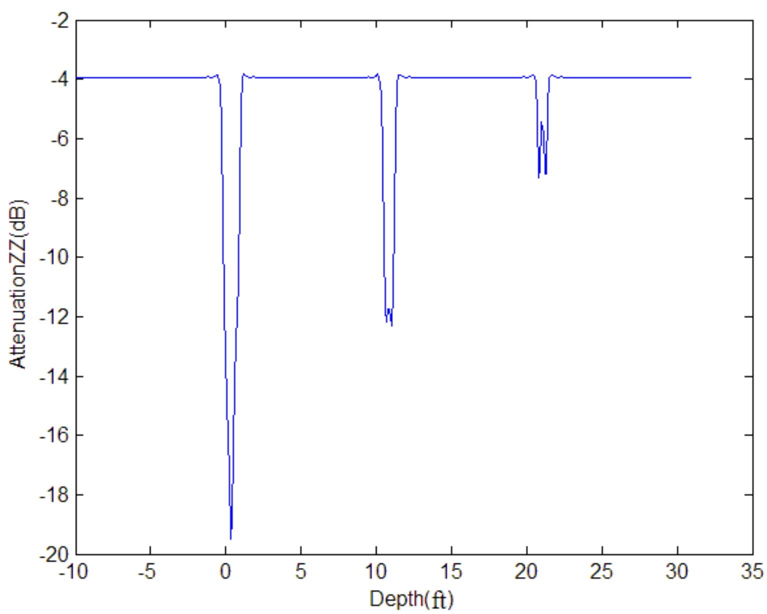

Figure 4.25. Attenuation of the *zz* component when frequency is 300 MHz.

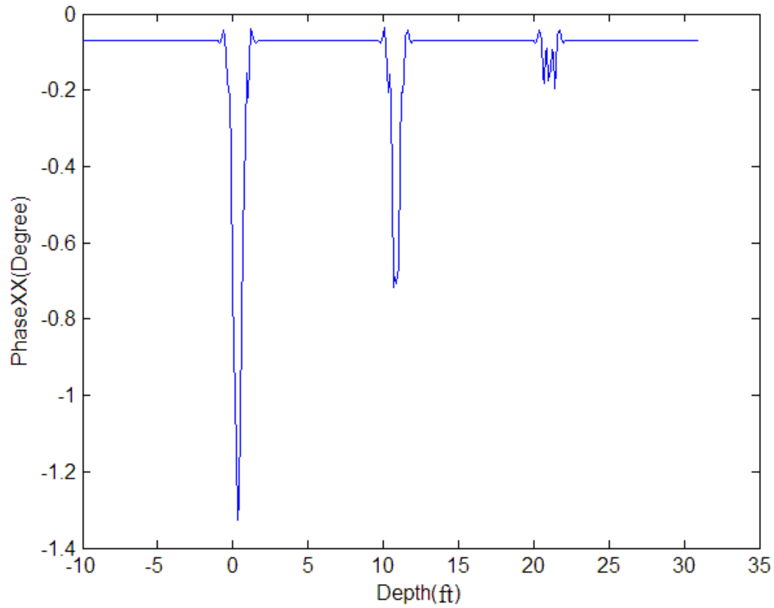

Figure 4.26. Phase shift of the *xx* component when frequency is 300 MHz.

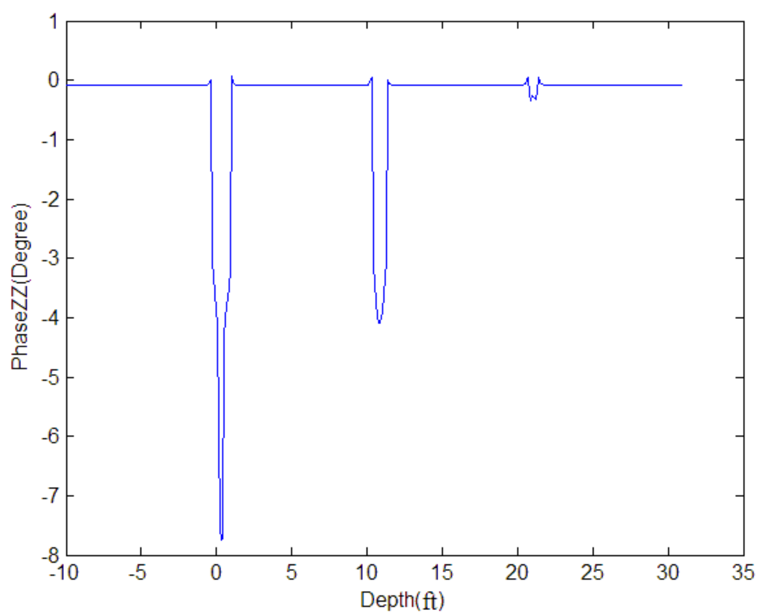

Figure 4.27. Phase shift of the *zz* component when frequency is 300 MHz.

4.2.2 400 MHz Frequency Results for the Dielectric Tool

Figures 4.28 and 4.29 show the attenuation of the *xx* and *zz* components for the 400 MHz frequency. Figures 4.30 and 4.31 show the phase shift of the *xx* and *zz* components for the 400 MHz frequency.

Considering that the layers are very thin, oscillations occur at the edge of each layer for the attenuation and phase shift. As frequency increases, the oscillation parts clearly occur. This phenomenon is caused by the fact that increasing frequency also increases the amplitude.

The phase shift of the *xx* component in the 8-inch layer changed its direction from negative to positive. However, its amplitude is also the highest among the three layers. The amplitude of the 1-inch layer is the smallest of the three layers for both attenuation and phase shift.

At this frequency, this simulation method can also calculate results with accuracy and fast speed. Thus, we will use a higher frequency to check the frequency limitation of this simulation method. The next part shows the 600 MHz frequency results.

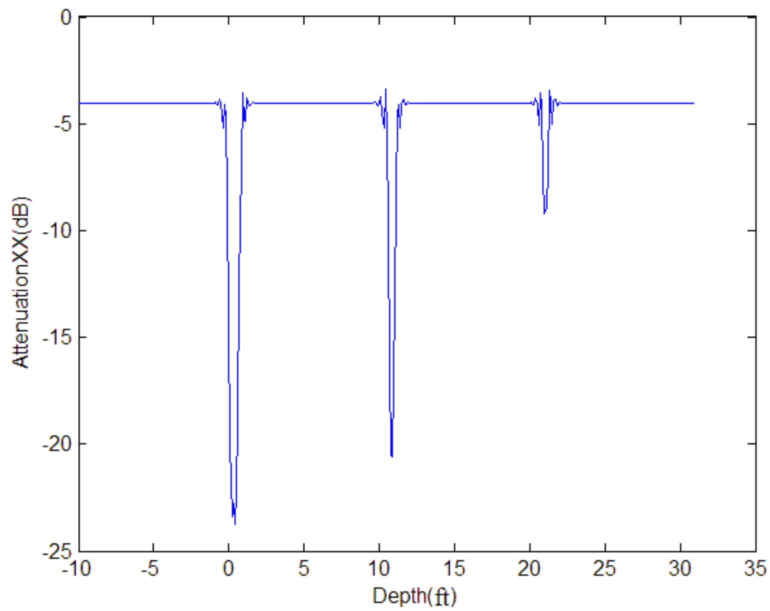

Figure 4.28. Attenuation of the *xx* component when frequency is 400 MHz.

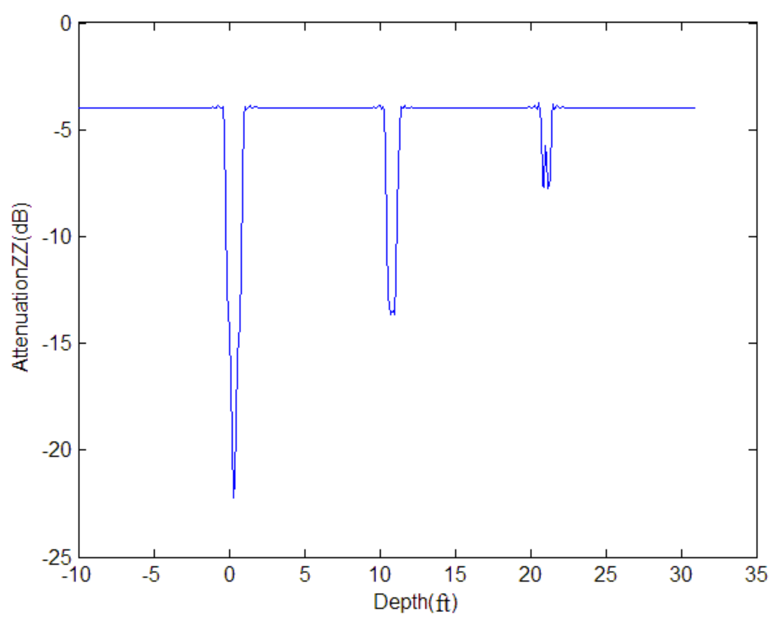

Figure 4.29. Attenuation of the *zz* component when frequency is 400 MHz.

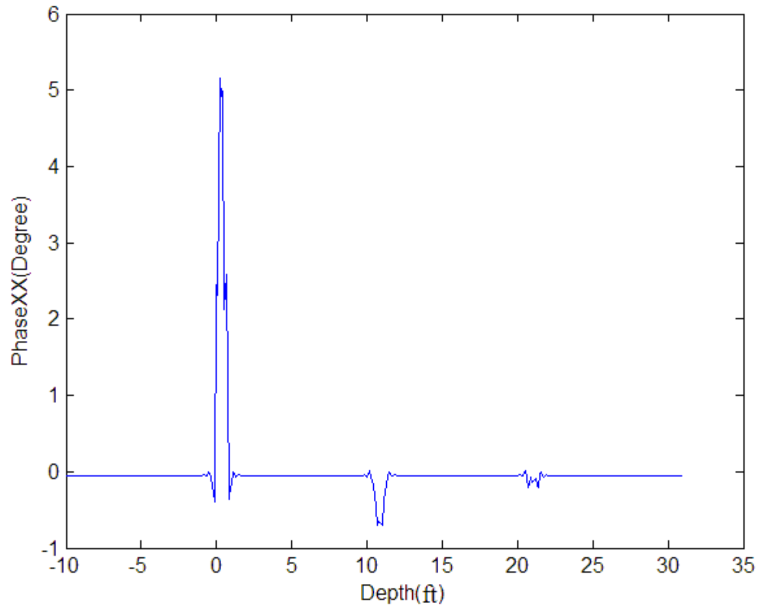

Figure 4.30. Phase shift of the *xx* component when frequency is 400 MHz.

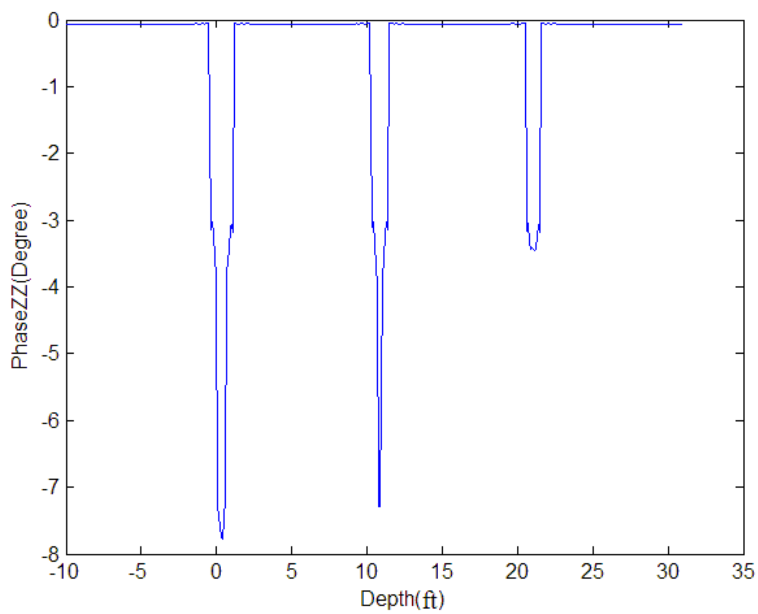

Figure 4.31. Phase shift of the *zz* component when frequency is 400 MHz.

4.2.3 600 MHz Frequency Results for the Dielectric Tool

Figures 4.32 and 4.33 show the attenuation of the *xx* and *zz* components for the 600 MHz frequency. Figures 4.34 and 4.35 show the phase shift of the *xx* and *zz* components for the 600 MHz frequency.

The oscillation parts occur more clearly than for frequencies lower than 600 MHz. For the attenuation of the *xx* and *zz* components, all the amplitudes for the three layers are higher than the 300 MHz and 400 MHz frequency results. The phase shift of the *xx* and *zz* components does not have this property.

The phase shift of the *zz* component can obtain a slightly unclear structure of the formation. However, we can identify the difference between the 8-inch layer and the 4-inch layer. The amplitude of the 8-inch layer is also the highest among the three layers. All these results for 600 MHz are good.

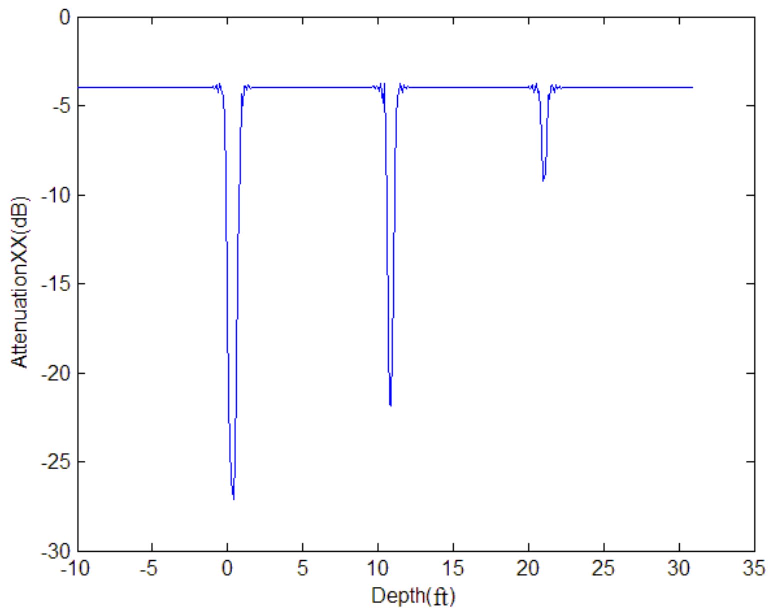

Figure 4.32. Attenuation of the *xx* component when frequency is 600 MHz.

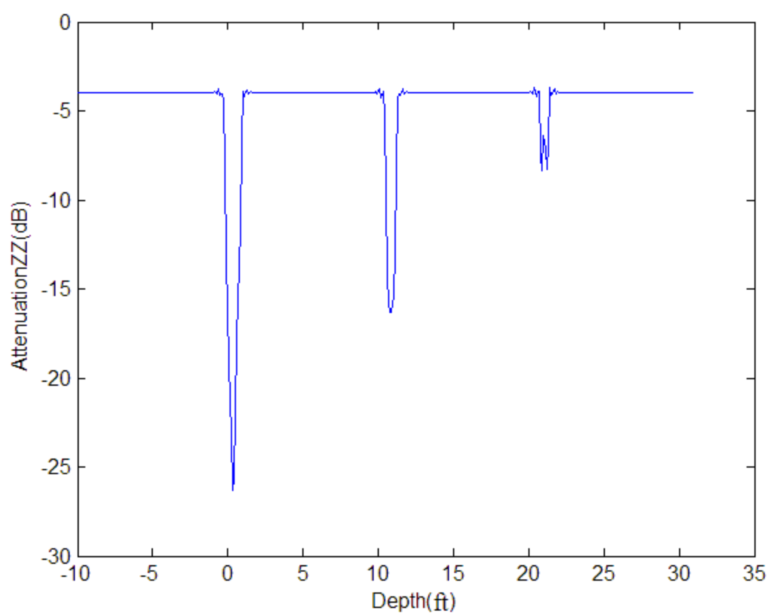

Figure 4.33. Attenuation of the *zz* component when frequency is 600 MHz.

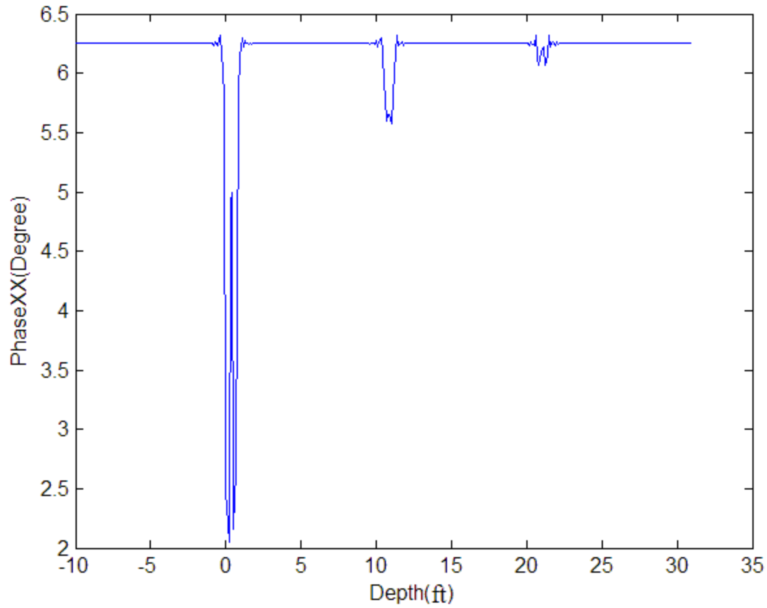

Figure 4.34. Phase shift of the *xx* component when frequency is 600 MHz.

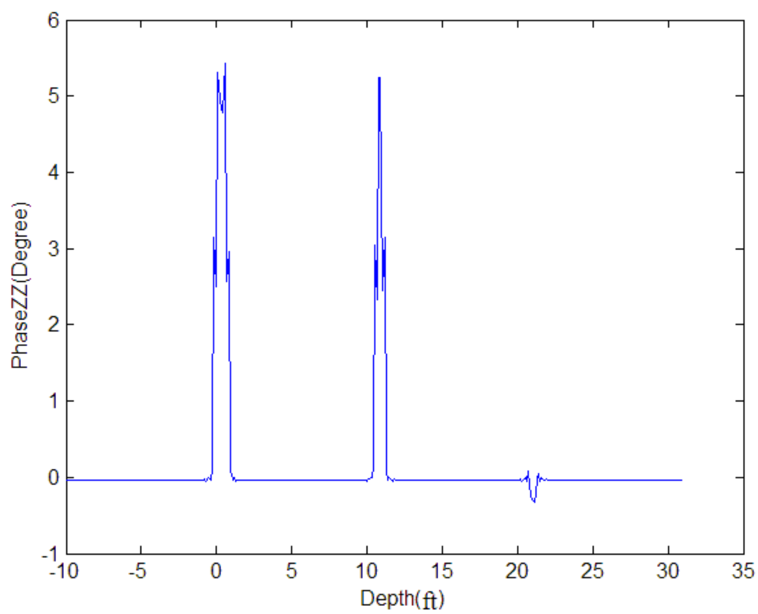

Figure 4.35. Phase shift of the *zz* component when frequency is 600 MHz.

4.2.4 700 MHz Frequency Results for the Dielectric Tool

Figures 4.36 and 4.37 show the attenuation of the *xx* and *zz* components for the 700 MHz frequency. Figures 4.38 and 4.39 show the phase shift of the *xx* and *zz* components for the 700 MHz frequency.

The oscillation parts occur more clearly than before. For the attenuation of the *xx* and *zz* components, all of the amplitudes for the three layers are higher than the 300 MHz, 400 MHz, and 600 MHz frequency results. The phase shift of the *xx* and *zz* components does not have this property.

The phase shift of the *zz* components is even worse than the 600 MHz frequency results. The amplitude for each layer is almost the same. However, we can identify the difference from the width of each layer. We can still obtain the structure of the formation from all the results.

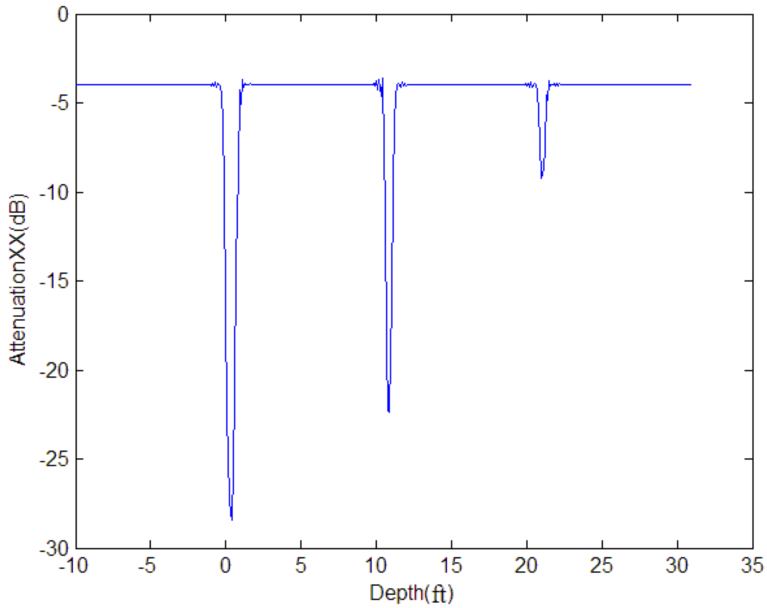

Figure 4.36. Attenuation of the *xx* component when frequency is 700 MHz.

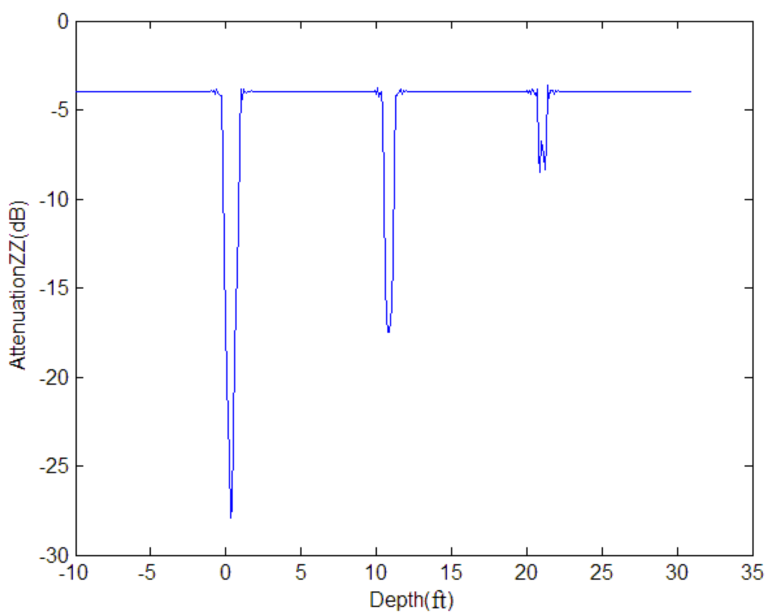

Figure 4.37. Attenuation of the *zz* component when frequency is 700 MHz.

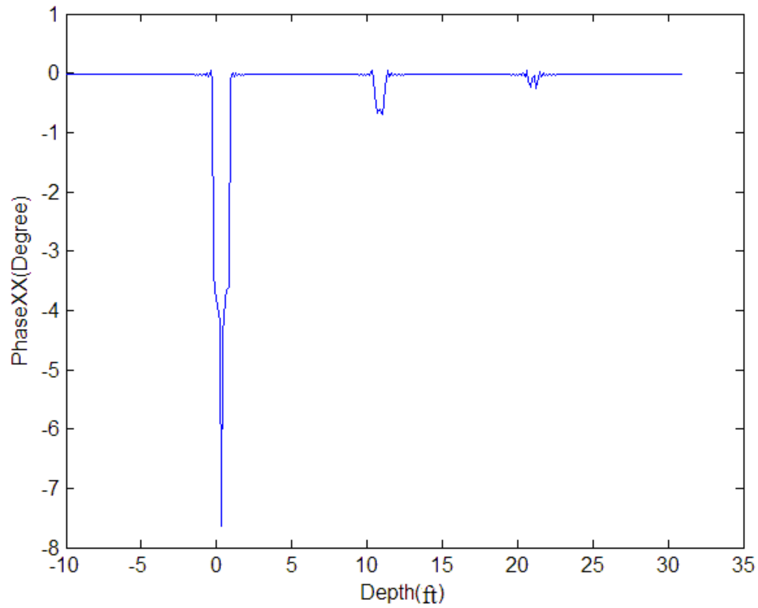

Figure 4.38. Phase shift of the *xx* component when frequency is 700 MHz.

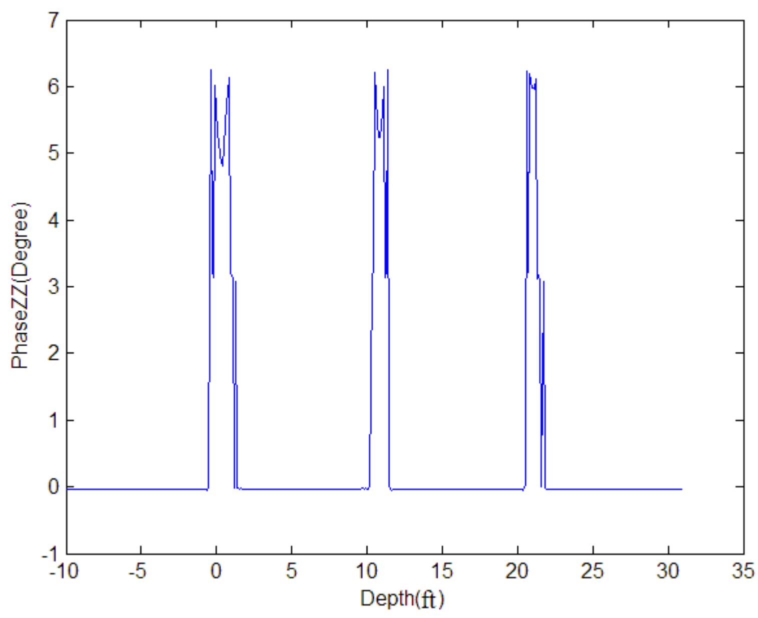

Figure 4.39. Phase shift of the *zz* component when frequency is 700 MHz.

4.2.5 800 MHz Frequency Results for the Dielectric Tool

Figures 4.40 and 4.41 show the attenuation of the *xx* and *zz* components for the 800 MHz frequency. Figures 4.42 and 4.43 show the phase shift of the *xx* and *zz* components for the 800 MHz frequency.

The oscillation parts occur more clearly than before. For the attenuation of the *xx* and *zz* components, all the amplitudes for the three layers are higher than before.

From all the results, we can clearly identify the structure of the formation. The results from the 800 MHz frequency are excellent. This simulation method can handle such a high frequency. We have to conduct more tests to check the frequency limitation.

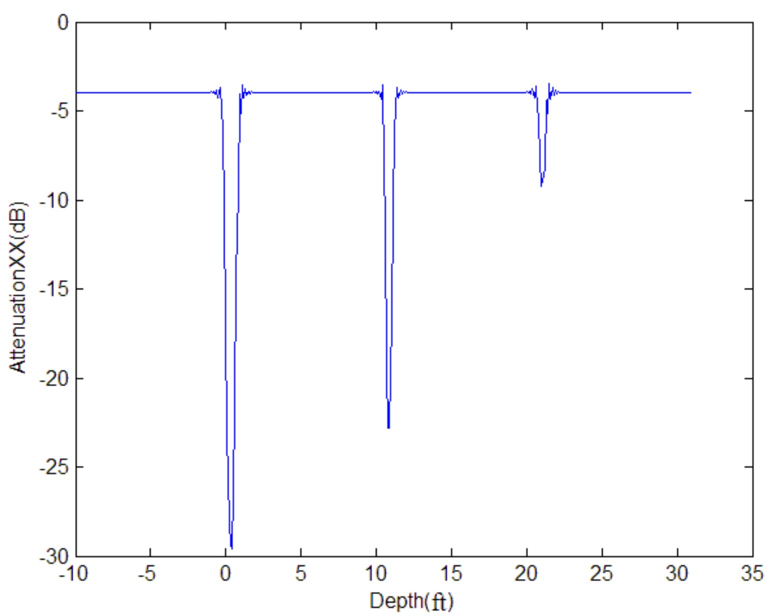

Figure 4.40. Attenuation of the *xx* component when frequency is 800 MHz.

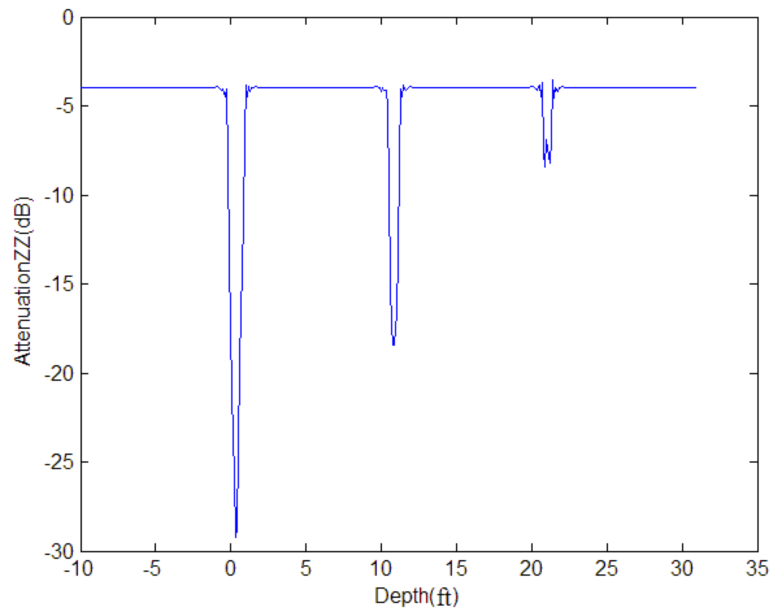

Figure 4.41. Attenuation of the *zz* component when frequency is 800 MHz.

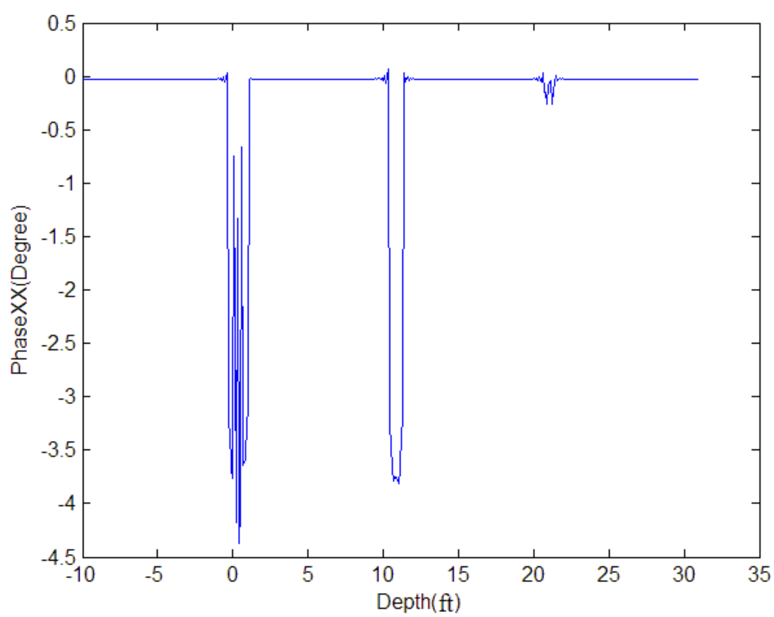

Figure 4.42. Phase shift of the *xx* component when frequency is 800 MHz.

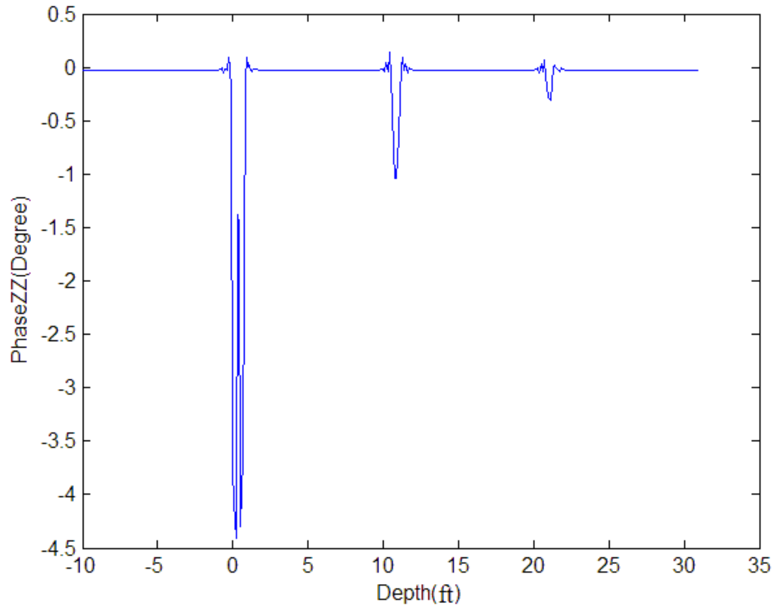

Figure 4.43. Phase shift of the *zz* component when frequency is 800 MHz.

4.2.6 900 MHz Frequency Results for the Dielectric Tool

Figures 4.44 and 4.45 show the attenuation of the *xx* and *zz* components for the 900 MHz frequency. Figures 4.46 and 4.47 show the phase shift of the *xx* and *zz* components for the 900 MHz frequency.

The oscillation parts occur more clearly than before. For the attenuation of *xx* and *zz* components, all the amplitudes for the three layers are higher than before.

The attenuation of the *xx* and *zz* components shows clear results of the structure of the formation. However, the phase shift of the *xx* component does not match the structure of the formation. From the result for the phase shift of the *xx* component, identifying the difference between a 4-inch thin layer and a 1-inch thin layer is difficult. The amplitudes of the 4 and 1-inch layers are almost the same. The width of the 4-inch layer is slightly larger than that of the 1-inch layer, but it is unclear.

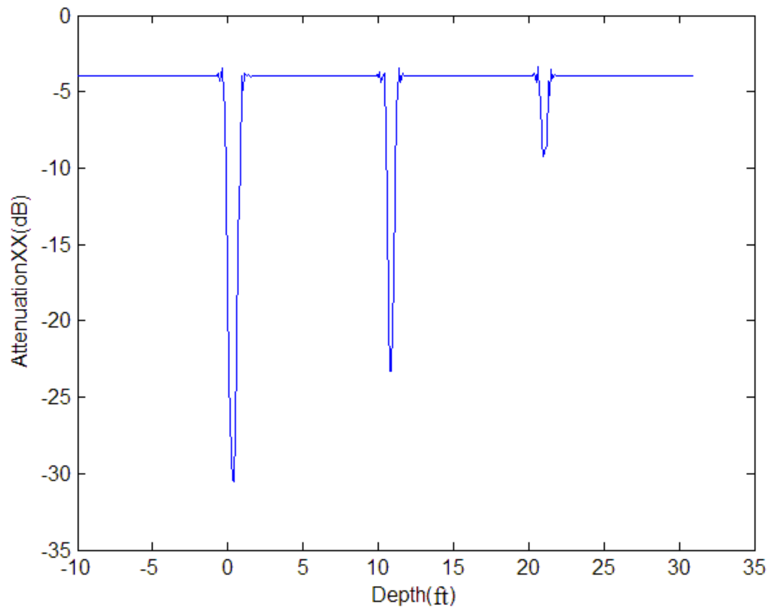

Figure 4.44. Attenuation of the *xx* component when frequency is 900 MHz.

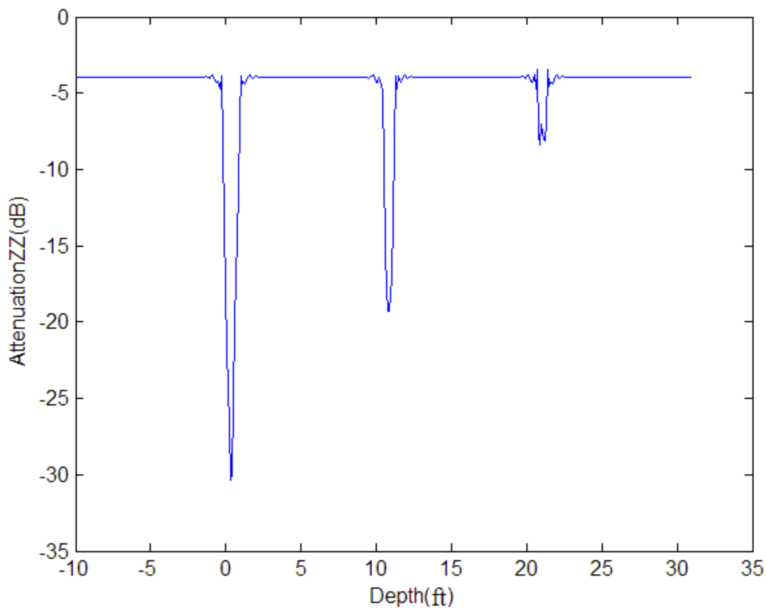

Figure 4.45. Attenuation of the *zz* component when frequency is 900 MHz.

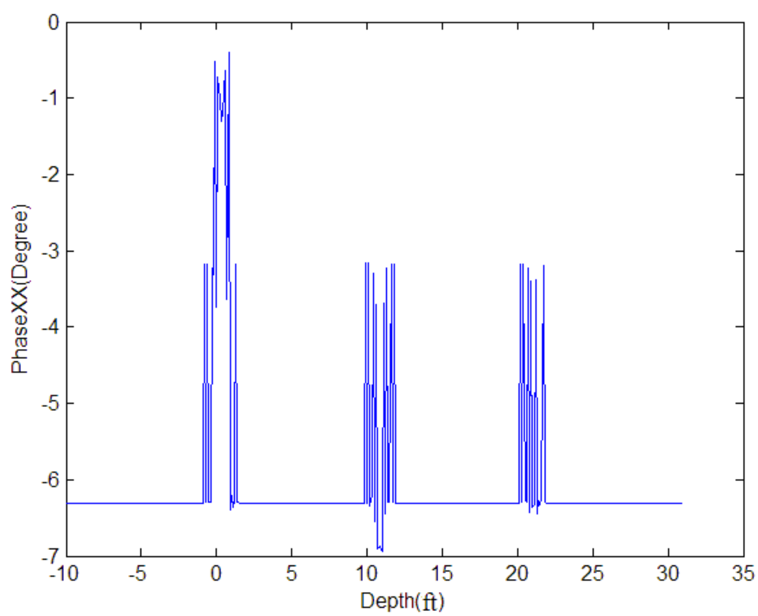

Figure 4.46. Phase shift of the *xx* component when frequency is 900 MHz.

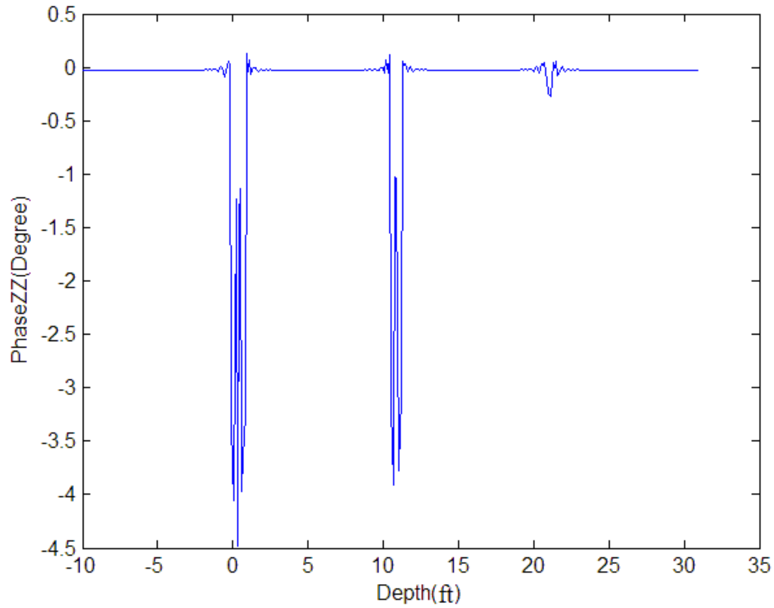

Figure 4.47. Phase shift of the *zz* component when frequency is 900 MHz.

4.2.7 1 GHz Frequency Results for the Dielectric Tool

Figures 4.48 and 4.49 show the attenuation of the *xx* and *zz* components for the 1 GHz frequency. Figures 4.50 and 4.51 show the phase shift of the *xx* and *zz* components for the 1 GHz frequency.

For such a high frequency, the attenuation of the *xx* and *zz* components can reflect the structure of the formation. However, the phase shift of the *xx* and *zz* components cannot reflect the structure of the formation. The phase shift of the *xx* component appears the same for the 8, 4, and 1-inch layers, but we can identify the difference from the width of the result. The phase shift of the *zz* component cannot identify the structure of the formation, and the amplitude of the 8-inch layer is lower than that of the 4-inch layer. This result is therefore bad.

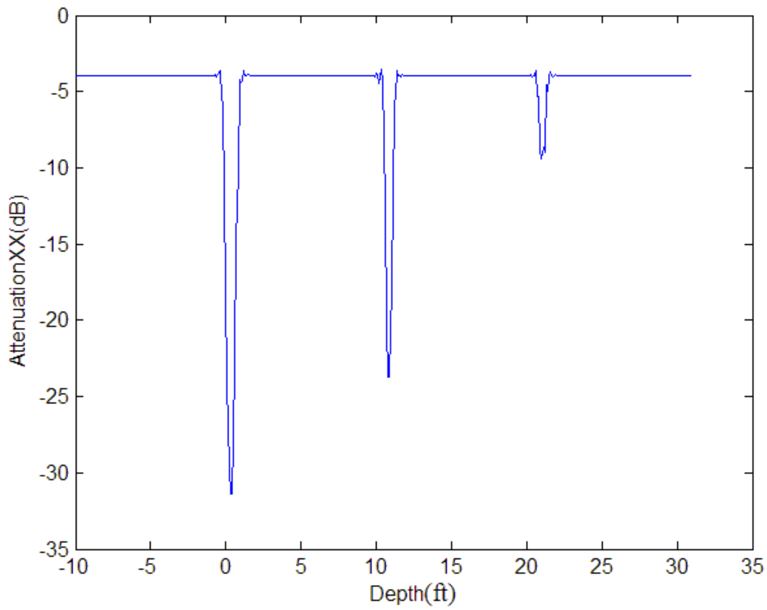

Figure 4.48. Attenuation of the *xx* component when frequency is 1 GHz.

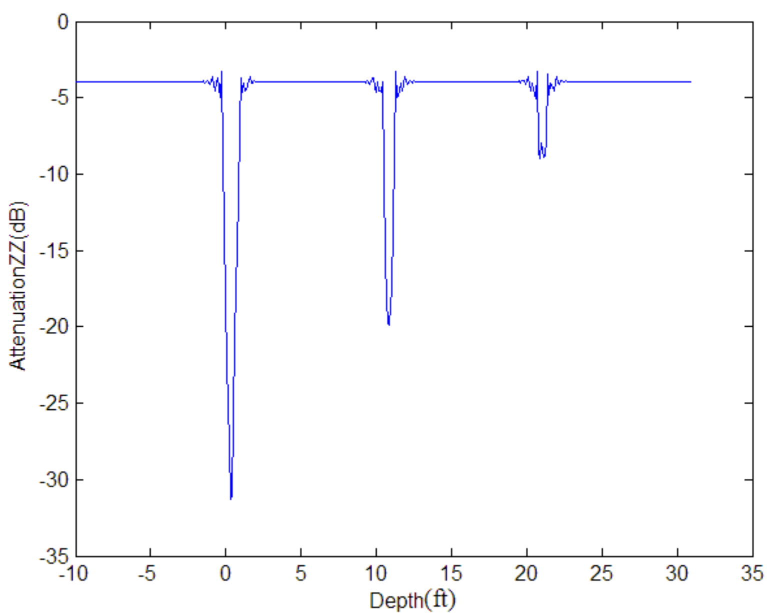

Figure 4.49. Attenuation of the *zz* component when frequency is 1 GHz.

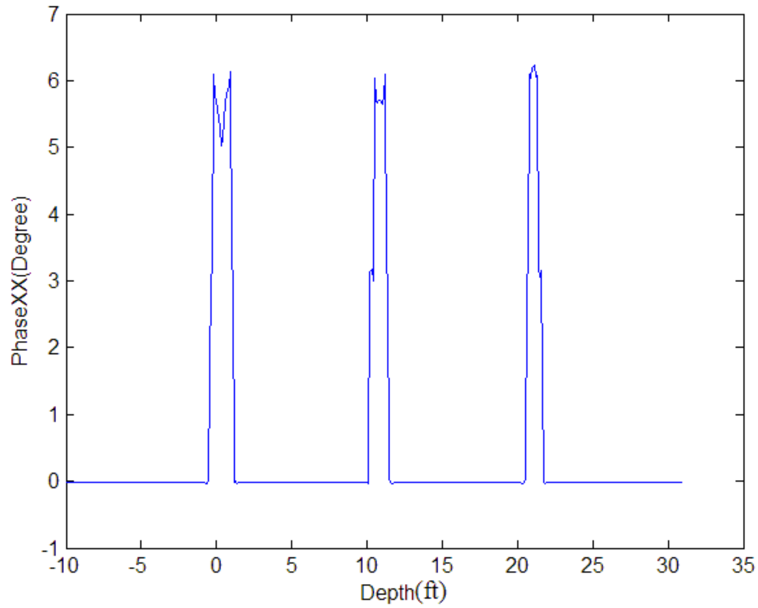

Figure 4.50. Phase shift of the *xx* component when frequency is 1 GHz.

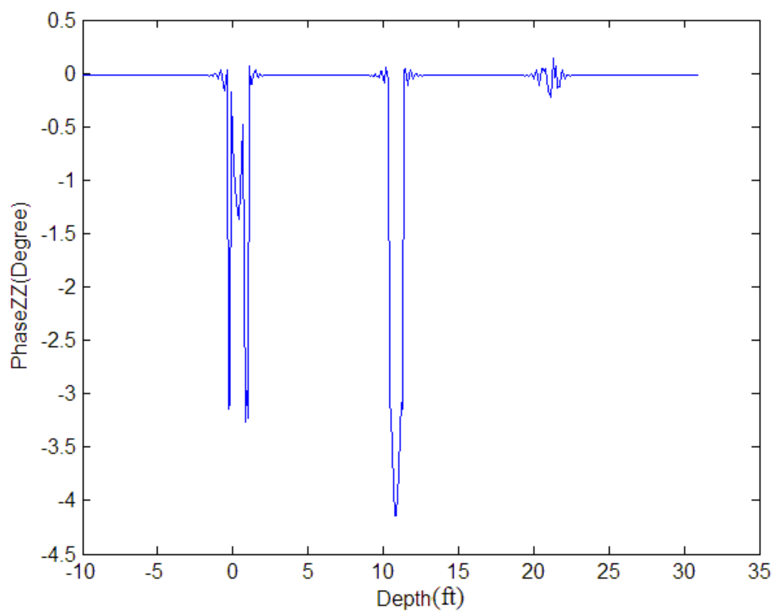

Figure 4.51. Phase shift of the *zz* component when frequency is 1 GHz.

4.3 Summary

All results show that at frequencies lower than 900 MHz, this simulation method can simulate a seven-layer formation with three thin layers with accuracy and fast speed. For frequencies higher than 900 MHz, some parts of the results show several errors, but we can still obtain the structure of the formation from the attenuation of the *xx* and *zz* components.

Therefore, the frequency limitation of this simulation is 900 MHz for accurate values. Higher frequencies require more filter weights for the fast Hankel transform method to calculate the infinite integral of the highly oscillatory Bessel function.

Chapter 5 Conclusion and Future Work

The simulation method in this thesis can handle the simulation for triaxial induction tools in a 1-D multi-layered transverse isotropic formation with fast speed and accuracy. Given that triaxial induction tools do not require extremely high frequencies, a100 MHz frequency is sufficient.

However for dielectric tools, which require high frequencies even up to 1 GHz, the simulation for a 1-D multi-layered transverse isotropic formation using this simulation method will not calculate results with accuracy.

Three properties can determine whether the results are good or not.

1. For good results, the amplitude of the same layer should increase as frequency increase.
2. For three different layers in the same frequency, the amplitude should decrease as the width of the layer decreases.
3. As the width of the layer decreases, the resulting width of each layer also decreases.

With these three properties, we can easily obtain the frequency limitation of the simulation method for dielectric tools.

From all the results obtained at different frequencies and tool spaces, the following conclusions can be drawn: First, when the frequency is low, the results from the simulation are very good. Thus, the formation can be accurately identified from the results. Second, if the frequency is high, such as 1 GHz, the results will not show accurate values but can show the structure of the formation. The reason for the error at high frequencies is because in the fast Hankel transform method, the filter weights are insufficient in handling the highly oscillatory Bessel function.

The next step for this project is to calculate more filter weights using the fast Hankel transform method. Thereafter, this simulation method can simulate dielectric tools with accuracy and fast speed.

References

[1] H. G. Doll (1949), “Introduction to Induction Logging and Application to Logging of Wells Drilled with Oil Base Mud,” *Journal of Petroleum Technology,* vol. 1, pp. 148-162.

[2] S. Calvert and T. Pritchard, *BG Group, Eric Decoster, Schlumberger,* 2006, “Tri-axial Array Induction Tool Aids Field Development for The North Coast Marine Area,” *SPWLA 47th Annual Logging Symposium*.

[3] K. S. Kunz and J. H. Moran (1958), “Some Effects of Formation Anisotropy on Resistivity Measurements in Boreholes,” *Geophysics,* vol. 23, pp. 770-794.

[4] J. D. Klein (1993), “Induction Log Anisotropy Corrections,” *Log Analyst*, vol. 34, no. 2, pp. 18–27.

[5] S. Graciet and L. C. Shen (1998), “Theory and Numerical Simulation of Induction and MWD Resistivity Tools in Anisotropic Dipping,” *Log Analyst*, vol. 39, no.1, pp. 24-37.

[6] M. Zhdanov, D. Kennedy, and E. Peksen (2001), “Foundations of Tensor Induction Well-logging,” *Petrophysics*, vol. 42, pp. 588–610.

[7] G. L. Wang, C. Torres-Verd ń, and S. Gianzero (2009), “Fast Simulation of Triaxial Borehole Induction Measurements Acquired in Axially Symmetrical and Transversely Isotropic Media,” *Geophysics*, vol. 74, no. 6, pp. 233–249.

[8] H. Wang, T. Barber, and K. Chen (2006), "Triaxial Induction Logging: Theory, Modeling, Inversion, and Interpretation," International Oil & Gas Conference and Exhibition in China, Beijing, China.

[9] M. J. Nam, D. Pardo, and C. Torres-Verdín (2010), "Simulation of Triaxial Induction Measurements in Dipping, Invaded, and Anisotropic Formations Using a Fourier Series Expansion in a Non–Orthogonal System of Coordinate Sand: A Self-adaptive Hp Finite-element Method," *Geophysics*, vol. 75, no. 3, pp. 83–95.

[10] B. Kriegshauser, Q. Fanini, S. Forgang, and G Itskovich (2000), "A New Multicomponent Induction Logging Tool to Resolve Anisotropic Formations," *SPWLA* 41st Annual Logging Symposium.

[11] A. B. Cheryauka and M. S. Zhdanov (2001), "Fast Modeling of a Tensor Induction Logging Response in a Horizontal Well in Inhomogeneous Anisotropic Formations," *SPWLA* 42nd Annual Logging Symposium.

[12] L. Yu , B. Kriegshauser, O. Fanini, and J. Xiao (2001), "A Fast Inversion Method for Multicomponent Induction Log Data," *SEG* 71st Annual International Meeting, Expanded Abstracts, pp. 361–364

[13] X. Lu, and D. Alumbaugh (2001), "One-dimensional Inversion of Three Component Induction Logging in Anisotropic Media," *SEG* 71st Annual International Meeting, Expanded Abstracts, pp. 376–380.

[14] Z. Zhang, L. Yu, B. Kriegshauser, and L. Tabarovsky (2004), "Determination of Relative Angles and Anisotropic Resistivity Using Multicomponent Induction Logging Data," *Geophysics*, vol. 69, 898–908.

[15] H. Wang, T. Barber, R. Rosthal, J. Tabanou, B. Anderson, and T. M. Habashy (2003), "Fast and Rigorous Inversion of Triaxial Induction Logging Data to Determine Formation Resistivity Anisotropy, Bed Boundary Position, Relative Dip and Azimuth Angles," *SEG* 73rd Annual International Meeting, Expanded Abstracts, pp. 514–517.

[16] A. G. Nekut (1994), "Anisotropic Induction Logging," *Geophysics*, vol. 59, pp.345-350.

[17] M. Huang, L. C. Shen (1989), "Computation of Induction Logs in Multiple-layer Dipping Formation," *IEEE* Transactions on Geosciences and Remote Sensing. vol. 27, no. 3.

[18] H. Wang, T. Barber, C. Morriss, R. Rosthal, R. Hayden, M. Markely (2006), "Determining Anisotropic Formation Resistivity at Any Relative Dip Using a Multiarray Triaxial Induction Tool," *SPE* Annual Technical Conference and Exhibition.

[19] J. E. Dennis, Jr. and R. B. Schnabel (1983), "Numerical Methods for Unconstrained Optimization and Nonlinear Equations," Prentice-Hall, Engle-wood Cliffs, New Jersey.

[20] M. Altman, J. Gill, and M. McDonald (2004), “Numerical Issues in Statistical Computing for the Social Scientist,” John Wiley & Sons, Inc, New Jersey.

[21] P. E. Gill and W. Murray (1974), “Newton-type Methods for Unconstrained and Linearly Constrained Optimization,” *Mathematical Programmin*g, no. 28, pp.31–350.

[22] P. E. Gill and W. Murray, and M. H. Wright (1981), “Practical Optimization,” Academic Press, London.

[23] R. Rosthal, T. Barber, S. Bonner, “Field Test Results of an Experimental Fully-triaxial Induction Tool,” *SPWLA* 44th Annual Logging Symposium.

[24] N. Yuan, X. C. Nie and R. Liu (2010), “Improvement of 1-D Simulation Codes for Induction, MWD and Triaxial Tools in Multi-layered Dipping Beds,” *Well Logging Laboratory Technical Report*, pp.32–71.

[25] M. J. Wilt, D. L. Alumbaugh, H. F. Morrison, A. Becker, K. H. Lee, and M. Deszcz-Pan (1995), “Crosswell Electromagnetic Tomography: System Design Considerations and Field Results,” *Geophysics*, vol. 60,no. 871–885.

[26] P. D. Fredericks, F. P. Hearn, and M. M. Wisler (1989), “Formation Evaluation While Drilling with a Dual Propagation Resistivity Tool,” *SPE* Annual Technical Conference and Exhibition.

[27] B. Anderson, T. Barber, and M. Luling (2006), “Observations of Large Dielectric Effects on Induction Logs, or Can Source Rocks Be Detected with Induction Measurements,” *SPWLA* 47th Annual Logging Symposium.

[28] B. Anderson, T. Barber, M. Luling, J. Rasmus, and P. Sen (2007), "Observations of Large Dielectric Effects on LWD Propagation-Resistivity Logs," *SPWLA* 48th Annual Logging Symposium.

[29] M. Hizem, H. Budan, B. Deville, O. Faivre, L. Mosse, and M. simon (2008), "Dielectric Dispersion: A New Wireline Petrophysical Measurement," Society of Petroleum Engineers.

[30] B. Anderson, T. Barber, and M. Luling (2006), "Observations of Large Dielectric Effects on Induction Logs, or Can Source Rocks Be Detected with Induction Measurements," Society of Petrophysicists and Well-Log Analysts.

[31] Ramos, Y., M. Chavez, U. D. Bustos, and E. Decoster (2012), "Reservoir Evaluation and Completion Optimization in Heavy Oil Sands with Dielectric and Diffusion Measurements," Society of Petroleum Engineers.

[32] Mosse, L., Carmona, R., Decoster, E., Faivre, O., Hizem, M., and Pasternack, E., (2009), "Dielectric Dispersion Logging in Heavy Oil: A Case Study from the Orinoco Belt," Society of Petrophysicists and Well-Log Analysts.

[33] Almarzooq, A., T. AlGhamdi, K. H. Sassi, and M. Badri (2013), "Characterization of Shale Gas Rocks Using Dielectric Dispersion and Nuclear Magnetic Resonance," Society of Petroleum Engineers.

[34] Altman, R., B. Anderson, J. Rasmus, and M. G. Luling (2008), "Dielectric Effects and Resistivity Dispersion on Induction and Propagation-Resistivity Logs in Complex

Volcanic Lithologies: A Case Study," Society of Petrophysicists and Well-Log Analysts.

[35] Grayson, S.T. and J.L. Hemingway (2013), "A Heavy Oil Mobility Quicklook Using Dielectric Measurements at Four Depths of Investigation," Society of Petroleum Engineers.

[36] Han, M., J. Cuadros, C. A. P. Suarez, E. Decoster, O. Faivre, L. Mosse, and N. Seleznev (2012), "Continous Estimate of Cation Exchange Capacity from Log Data: A New Approach Based on Dielectric Dispersion Analysis," Society of Petrophysicists and Well-Log Analysts.

[37] Schmitt, D.P., A. AI-Harbi, P. Saldungaray, R. Akkurt, and T. Zhang (2011), "Revisiting Dielectric Logging in Saudi Arabia: Recent Experiences and Applications in Development and Exploration Wells," Society of Petroleum Engineers.

Appendix I. Derivation of Hertz Vector Potential in Multiple Layer Formation

I.1 *x*-directed Magnetic Dipole

A horizontally oriented magnetic dipole $\boldsymbol{M} = (\mathrm{M_x}, 0, 0)^T$ is assumed. According to Equation (2), we can obtain two new scalar equations as follows:

$$\nabla_\lambda^2 \pi_x + k_v^2 \pi_x = -\frac{1}{\lambda^2} M_x \tag{A.1}$$

and

$$\nabla^2 \pi_z + k_h^2 \pi_z = \left(1-\lambda^2\right) \frac{\partial^2 \pi_x}{\partial z \partial x}, \tag{A.2}$$

where $\nabla_\lambda^2 = \left(\frac{\partial^2}{\partial x^2} + \frac{\partial^2}{\partial y^2} + \frac{1}{\lambda^2} \frac{\partial^2}{\partial z^2} \right)$, and $k_v^2 = i\omega\mu_0\sigma_v$.

In order to get the solution of Equation (A.1), we first consider the homogeneous equation with zero on the right-hand sides:

$$\nabla_\lambda^2 \pi_x + k_v^2 \pi_x = 0. \tag{A.3}$$

The Hertz potential π_x can be expressed as

$$\pi_x = \int_0^\infty F(z) \alpha J_0\left(\alpha\rho\right) d\alpha. \tag{A.4}$$

Since $\nabla_\lambda^2 \pi_x = \frac{\partial^2 \pi_x}{\partial x^2} + \frac{\partial^2 \pi_x}{\partial y^2} + \frac{\partial^2 \pi_x}{\lambda^2 \partial z^2}$, we first derive $\frac{\partial^2 \pi_x}{\partial x^2}$, and

$$\frac{\partial^2 \pi_x}{\partial x^2} = \int_0^\infty F(z) \alpha \frac{\partial^2 J_0\left(\alpha\rho\right)}{\partial x^2} d\alpha. \tag{A.5}$$

It is easy to get

$$\frac{\partial^2 J_0(\alpha\rho)}{\partial x^2} = -\frac{\alpha J_1(\alpha\rho)}{\rho} + \frac{2\alpha x^2 J_1(\alpha\rho)}{\rho^3} - \frac{\alpha^2 x^2 J_0(\alpha\rho)}{\rho^2}. \tag{A.6}$$

Then we derive

$$\frac{\partial^2 \pi_x}{\partial x^2} = \int_0^\infty \left[-\frac{\alpha J_1(\alpha\rho)}{\rho} + \frac{2\alpha x^2 J_1(\alpha\rho)}{\rho^3} - \frac{\alpha^2 x^2}{\rho^2} J_0(\alpha\rho) \right] \alpha F(z) d\alpha. \tag{A.7}$$

Similarly, we obtain $\frac{\partial^2 \pi_x}{\partial y^2}$ as

$$\frac{\partial^2 \pi_x}{\partial y^2} = \int_0^\infty \left[-\frac{\alpha J_1(\alpha\rho)}{\rho} + \frac{2\alpha y^2 J_1(\alpha\rho)}{\rho^3} - \frac{\alpha^2 y^2}{\rho^2} J_0(\alpha\rho) \right] \alpha F(z) d\alpha. \tag{A.8}$$

On the other hand, we know

$$\frac{\partial^2 \pi_x}{\lambda^2 \partial z^2} = \int_0^\infty \frac{\partial^2 F(z)}{\lambda^2 \partial z^2} \alpha J_0(\alpha\rho) d\alpha. \tag{A.9}$$

Therefore,

$$\begin{aligned}
\nabla_\lambda^2 \pi_x + k_v^2 \pi_x &= \int_0^\infty \left[-\frac{\alpha J_1(\alpha\rho)}{\rho} + \frac{2\alpha x^2 J_1(\alpha\rho)}{\rho^3} - \frac{\alpha^2 x^2}{\rho^2} J_0(\alpha\rho) \right] \alpha F(z) d\alpha + \\
&\int_0^\infty \left[-\frac{\alpha J_1(\alpha\rho)}{\rho} + \frac{2\alpha y^2 J_1(\alpha\rho)}{\rho^3} - \frac{\alpha^2 y^2}{\rho^2} J_0(\alpha\rho) \right] \alpha F(z) d\alpha + \\
&\int_0^\infty \frac{\partial^2 F(z)}{\lambda^2 \partial z^2} \alpha J_0(\alpha\rho) d\alpha + k_v^2 \int_0^\infty F(z) \alpha J_0(\alpha\rho) d\alpha \\
&= \int_0^\infty \left(-\alpha^2 + k_v^2 \right) J_0(\alpha\rho) \alpha F(z) d\alpha + \int_0^\infty \frac{\partial^2 F(z)}{\lambda^2 \partial z^2} \alpha J_0(\alpha\rho) d\alpha \\
&= \int_0^\infty \left(-\xi_v^2 F(z) + \frac{\partial^2 F(z)}{\lambda^2 \partial z^2} \right) \alpha J_0(\alpha\rho) d\alpha \\
&= 0.
\end{aligned} \tag{A.10}$$

Then we obtain

$$F(z)=\frac{M_x}{4\pi\lambda}\left(Pe^{-\xi_v\lambda z}+Qe^{\xi_v\lambda z}\right). \tag{A.11}$$

We consider the constant number $\frac{M_x}{4\pi\lambda}$ for convenience of expression. The solution of Equation (A.3) is in the form

$$\pi_{x,g}=\frac{M_x}{4\pi\lambda}\int_0^\infty\left(P\,e^{-\xi_v\lambda\, z}+Q\,e^{\xi_v\lambda\, z}\right)\alpha J_0(\alpha\rho)d\alpha\,, \tag{A.12}$$

where $\pi_{x,g}$ represents a general solution.

The particular solution of Equation (A.1) is well known:

$$\pi_{x,p}=\frac{M_x}{4\pi\lambda}\frac{e^{ik_v s}}{s}=\frac{M_x}{4\pi\lambda}\int_0^\infty\frac{1}{\xi_v}e^{-\xi_v\lambda|z-z_0|}\alpha J_0(\alpha\rho)d\alpha\,. \tag{A.13}$$

The final solution of Equation (A.1) is found to be

$$\pi_x=\pi_{x,g}+\pi_{x,p}=\frac{M_x}{4\pi\lambda}\int_0^\infty\left(\frac{1}{\xi_v}e^{-\xi_v\lambda|z-z_0|}+P\,e^{-\xi_v\lambda\, z}+Q\,e^{\xi_v\lambda\, z}\right)\alpha J_0(\alpha\rho)d\alpha\,. \tag{A.14}$$

Next, let us see how to solve Equation (A.2),

$$\nabla^2\pi_z+k_h^2\pi_z=\left(1-\lambda^2\right)\frac{\partial^2\left(\pi_{x,g}+\pi_{x,p}\right)}{\partial z\partial x}\ =\left(1-\lambda^2\right)\frac{\partial^2\pi_{x,g}}{\partial z\partial x}+\left(1-\lambda^2\right)\frac{\partial^2\pi_{x,p}}{\partial z\partial x}\,. \tag{A.15}$$

Now we rewrite Equation (A.15) into two independent Equations as follows:

$$\nabla^2\pi_{z,g}+k_h^2\pi_{z,g}=\left(1-\lambda^2\right)\frac{\partial^2\pi_{x,g}}{\partial z\partial x} \tag{A.16}$$

and

$$\nabla^2 \pi_{z,p} + k_h^2 \pi_{z,p} = \left(1-\lambda^2\right)\frac{\partial^2 \pi_{x,p}}{\partial z \partial x} . \tag{A.17}$$

Note: The solution of Equation (A.15) should be the sum of $\pi_{z,g}, \pi_{z,p}$.

First, we solve for $\pi_{z,g}$. Let

$$\pi_{z,g} = \frac{x}{\rho}\frac{M_x}{4\pi}\int_0^\infty E(z) J_1\left(\alpha\rho\right) d\alpha = -\frac{\partial}{\partial x}\frac{M_x}{4\pi}\int_0^\infty \frac{E(z)}{\alpha} J_0\left(\alpha\rho\right) d\alpha . \tag{A.18}$$

Then we know

$$\begin{aligned}\frac{\partial^2 \pi_{z,g}}{\partial x^2} &= -\frac{\partial}{\partial x}\frac{M_x}{4\pi}\int_0^\infty \frac{E(z)}{\alpha}\frac{\partial^2 J_0\left(\alpha\rho\right)}{\partial x^2} d\alpha \\ &= \frac{\partial}{\partial x}\frac{M_x}{4\pi}\int_0^\infty E(z)\left[\frac{1}{\rho}J_1\left(\alpha\rho\right) + \frac{\alpha x^2}{\rho^2}J_0\left(\alpha\rho\right) - \frac{2x^3}{\rho^3}J_1\left(\alpha\rho\right)\right] d\alpha\end{aligned} , \tag{A.19}$$

$$\begin{aligned}\frac{\partial^2 \pi_{z,g}}{\partial y^2} &= -\frac{\partial}{\partial x}\frac{M_x}{4\pi}\int_0^\infty \frac{E(z)}{\alpha}\frac{\partial^2 J_0\left(\alpha\rho\right)}{\partial y^2} d\alpha \\ &= \frac{\partial}{\partial x}\frac{M_x}{4\pi}\int_0^\infty E(z)\left[\frac{1}{\rho}J_1\left(\alpha\rho\right) + \frac{\alpha y^2}{\rho^2}J_0\left(\alpha\rho\right) - \frac{2y^3}{\rho^3}J_1\left(\alpha\rho\right)\right] d\alpha\end{aligned} \text{, and} \tag{A.20}$$

$$\frac{\partial^2 \pi_{z,g}}{\partial z^2} = -\frac{\partial}{\partial x}\frac{M_x}{4\pi}\int_0^\infty \frac{d^2E(z)}{\alpha dz^2} J_0\left(\alpha\rho\right) d\alpha . \tag{A.21}$$

Therefore,

$$\nabla^2 \pi_{z,g} + k_h^2 \pi_{z,g} = \frac{\partial}{\partial x}\frac{M_x}{4\pi}\int_0^\infty \left[\frac{E(z)}{\alpha}\xi_h^2 J_0\left(\alpha\rho\right) - \frac{d^2E(z)}{\alpha dz^2}J_0\left(\alpha\rho\right)\right] d\alpha . \tag{A.22}$$

We can derive

$$\left(1-\lambda^2\right)\frac{\partial^2\pi_{x,p}}{\partial z\partial x}=\left(1-\lambda^2\right)\frac{\partial}{\partial x}\frac{M_x}{4\pi\lambda}\int_0^\infty\left(\xi_v\lambda Pe^{-\xi_v\lambda z}+\xi_v\lambda Qe^{\xi_v\lambda z}\right)\alpha J_0(\alpha\rho)d\alpha\,. \quad (A.23)$$

Since

$$\frac{\partial}{\partial x}\frac{M_x}{4\pi}\int_0^\infty\left[\frac{E(z)}{\alpha}\xi_h^2-\frac{d^2E(z)}{\alpha dz^2}\right]J_0(\alpha\rho)d\alpha=\left(1-\lambda^2\right)\frac{\partial}{\partial x}\frac{M_x}{4\pi\lambda}\int_0^\infty\left(Pe^{-\xi_v\lambda z}+Qe^{\xi_v\lambda z}\right)\xi_v\lambda\alpha J_0(\alpha\rho)d\alpha,$$

(A.24)

then we obtain a new equation for $E(z)$ as follows:

$$\frac{d^2E(z)}{dz^2}-E(z)\xi_h^2=\left(1-\lambda^2\right)\left(Pe^{-\xi_v\lambda z}-Qe^{\xi_v\lambda z}\right)\xi_v\alpha^2. \quad (A.25)$$

The solution of the Equation (A.25) is in the form

$$E(z)=Se^{-\xi_h z}+Te^{\xi_h z}+E^*(z)\,. \quad (A.26)$$

$E^*(z)$ is the specific solution of $E(z)$. We apply the constant variation method to obtain $E^*(z)$. Let

$$E^*(z)=S(z)e^{-\xi_h z}+T(z)e^{\xi_h z}\,. \quad (A.27)$$

Then $S(z),T(z)$ should satisfy these linear equations:

$$S^{'}(z)e^{-\xi_h z}+T^{'}(z)e^{\xi_h z}=0 \quad (A.28)$$

and

$$S^{'}(z)(-\xi_h)e^{-\xi_h z}+T^{'}(z)\xi_h e^{\xi_h z}=\left(1-\lambda^2\right)\left(Pe^{-\xi_v\lambda z}-Qe^{\xi_v\lambda z}\right)\xi_v\alpha^2. \quad (A.29)$$

Then we obtain

$$S(z)=-\frac{\left(1-\lambda^2\right)\alpha^2\xi_v}{2\xi_h}\left[\frac{Pe^{-\xi_v\lambda z+\xi_h z}}{-\xi_v\lambda+\xi_h}-\frac{Qe^{\xi_v\lambda z+\xi_h z}}{\xi_v\lambda+\xi_h}\right]$$
$$=-\frac{\left(1-\lambda^2\right)\alpha^2\xi_v}{2\xi_h\left(\xi_h^2-\xi_v^2\lambda^2\right)}\left[Pe^{-\xi_v\lambda z+\xi_h z}\left(\xi_v\lambda+\xi_h\right)-Qe^{\xi_v\lambda z+\xi_h z}\left(-\xi_v\lambda+\xi_h\right)\right] \tag{A.30}$$

and

$$T(z)=\frac{\left(1-\lambda^2\right)\alpha^2\xi_v}{2\xi_h}\left[\frac{Pe^{-\xi_v\lambda z-\xi_h z}}{-\xi_v\lambda-\xi_h}-\frac{Qe^{\xi_v\lambda z-\xi_h z}}{\xi_v\lambda-\xi_h}\right]$$
$$=\frac{\left(1-\lambda^2\right)\alpha^2\xi_v}{2\xi_h\left(\xi_h^2-\xi_v^2\lambda^2\right)}\left[Pe^{-\xi_v\lambda z+\xi_h z}\left(\xi_v\lambda-\xi_h\right)-Qe^{\xi_v\lambda z+\xi_h z}\left(-\xi_v\lambda-\xi_h\right)\right]. \tag{A.31}$$

Since

$$\frac{\left(1-\lambda^2\right)\alpha^2}{\xi_h^2-\xi_v^2\lambda^2}=\frac{\left(1-\lambda^2\right)\alpha^2}{\left(\alpha^2-k_h^2\right)-\left(\alpha^2-k_v^2\right)\lambda^2}$$
$$=\frac{\left(1-\lambda^2\right)\alpha^2}{\left(\alpha^2-\alpha^2\lambda^2\right)-\left(k_h^2-k_v^2\lambda^2\right)}, \tag{A.32}$$
$$=\frac{\left(1-\lambda^2\right)\alpha^2}{\left(\alpha^2-\alpha^2\lambda^2\right)-\left(k_h^2-k_h^2\right)}$$
$$=1$$

therefore

$$S(z)=-\frac{\xi_v}{2\xi_h}\left[Pe^{-\xi_v\lambda z+\xi_h z}\left(\xi_v\lambda+\xi_h\right)-Qe^{\xi_v\lambda z+\xi_h z}\left(-\xi_v\lambda+\xi_h\right)\right] \tag{A.33}$$

and

$$T(z)=\frac{\xi_v}{2\xi_h}\left[Pe^{-\xi_v\lambda z+\xi_h z}\left(\xi_v\lambda-\xi_h\right)-Qe^{\xi_v\lambda z+\xi_h z}\left(-\xi_v\lambda-\xi_h\right)\right]. \tag{A.34}$$

Then $E^*(z)$ is

$$E^*(z) = S(z)e^{-\xi_h z} + T(z)e^{\xi_h z} = \xi_v\left[-Pe^{-\xi_v \lambda z} + Qe^{\xi_v \lambda z}\right]. \tag{A.35}$$

The solution of the Equation (A.25) is in the form:

$$E(z) = Se^{-\xi_h z} + Te^{\xi_h z} + \xi_v\left[-Pe^{-\xi_v \lambda z} + Qe^{\xi_v \lambda z}\right]. \tag{A.36}$$

Therefore, it is known

$$\pi_{z,g} = \frac{x}{\rho}\frac{M_x}{4\pi}\int_0^\infty \left[Se^{-\xi_h z} + Te^{\xi_h z} + \xi_v\left(-Pe^{-\xi_v \lambda z} + Qe^{\xi_v \lambda z}\right)\right] J_1(\alpha\rho)\, d\alpha\ . \tag{A.37}$$

Next, we need to derive $\pi_{z,p}$. Let

$$\pi_{z,p} = \frac{x}{\rho}\frac{M_x}{4\pi}\int_0^\infty C(z) J_1(\alpha\rho)\, d\alpha = -\frac{\partial}{\partial x}\frac{M_x}{4\pi}\int_0^\infty \frac{C(z)}{\alpha} J_0(\alpha\rho)\, d\alpha\ . \tag{A.38}$$

Similarly, we get

$$\nabla^2 \pi_{z,p} + k_h^2 \pi_{z,p} = \frac{\partial}{\partial x}\frac{M_x}{4\pi}\int_0^\infty \left[C(z)\xi_h^2 - \frac{d^2 C(z)}{dz^2}\right]\frac{J_0(\alpha\rho)}{\alpha}\, d\alpha \tag{A.39}$$

and

$$\frac{\partial \pi_{x,p}}{\partial z} = -\frac{M_x}{4\pi}\int_0^\infty \frac{|z-z_0|}{z-z_0} e^{-\xi_v \lambda |z-z_0|} \alpha J_0(\alpha\rho)\, d\alpha\ . \tag{A.40}$$

It is known that

$$\frac{\partial}{\partial x}\frac{M_x}{4\pi}\int_0^\infty \left[C(z)\xi_h^2 - \frac{d^2 C(z)}{dz^2}\right]\frac{J_0(\alpha\rho)}{\alpha}\, d\alpha = -\frac{\partial}{\partial x}\frac{M_x}{4\pi}\int_0^\infty \frac{|z-z_0|}{z-z_0} e^{-\xi_v \lambda |z-z_0|} \alpha J_0(\alpha\rho)\, d\alpha\ . \tag{A.41}$$

A new equation is thus obtained as

$$\frac{d^2C(z)}{dz^2} - C(z)\xi_h^2 = \left(\lambda^2 - 1\right)\frac{|z - z_0|}{z - z_0} e^{-\xi_v \lambda |z - z_0|}\alpha^2 . \tag{A.42}$$

Similarly, we apply the constant variance method to get $C(z)$, as follows:

$$C(z) = Ae^{-\xi_h |z - z_0|} + Be^{\xi_h |z - z_0|} - \frac{|z - z_0|}{z - z_0} e^{-\xi_v \lambda |z - z_0|} . \tag{A.43}$$

Then we choose $A = \frac{|z - z_0|}{z - z_0}$, $B = 0$ according to the boundary conditions of the homogenous formation.

The particular solution is in the form:

$$\pi_{z,p} = \frac{x}{\rho}\frac{M_x}{4\pi}\int_0^\infty \frac{|z - z_0|}{z - z_0}\left(e^{-\xi_h |z - z_0|} - e^{-\xi_v \lambda |z - z_0|}\right) J_1\left(\alpha\rho\right) d\alpha . \tag{A.44}$$

The final solution is

$$\begin{aligned} \pi_z = {} & \frac{x}{\rho}\frac{M_x}{4\pi}\int_0^\infty \left[Se^{-\xi_h z} + Te^{\xi_h z} + \xi_v\left(-Pe^{-\xi_v \lambda z} + Qe^{\xi_v \lambda z}\right)\right] J_1\left(\alpha\rho\right) d\alpha + \\ & \frac{x}{\rho}\frac{M_x}{4\pi}\int_0^\infty \frac{|z - z_0|}{z - z_0}\left(e^{-\xi_h |z - z_0|} - e^{-\xi_v \lambda |z - z_0|}\right) J_1\left(\alpha\rho\right) d\alpha \end{aligned} . \tag{A.45}$$

I.2 *y*-directed Magnetic Dipole

For an *x*-directed dipole, the Hertz vector potential can be similarly obtained as

$$\pi_y = \frac{M_y}{4\pi\lambda}\int_0^\infty \left(\frac{1}{\xi_v} e^{-\xi_v \lambda |z - z_0|} + Pe^{-\xi_v \lambda z} + Qe^{\xi_v \lambda z} \right)\alpha J_0(\alpha\rho) d\alpha \tag{A.46}$$

and

$$\pi_z = \frac{y}{\rho}\frac{M_y}{4\pi}\int_0^\infty \left[Se^{-\xi_h z} + Te^{\xi_h z} + \xi_v \left(-Pe^{-\xi_v \lambda z} + Qe^{\xi_v \lambda z} \right) \right] J_1(\alpha\rho)\, d\alpha + \\ \frac{y}{\rho}\frac{M_y}{4\pi}\int_0^\infty \frac{|z - z_0|}{z - z_0} \left(e^{-\xi_h |z - z_0|} - e^{-\xi_v \lambda |z - z_0|} \right) J_1(\alpha\rho)\, d\alpha \quad . \tag{A.47}$$

I.3 *z*-directed Magnetic Dipole

A horizontally oriented magnetic dipole $\boldsymbol{M} = (0, 0, M_z)^T$ is assumed. According to Equation (2),

$$\nabla^2 \pi_z + k_h^2 \pi_z = -M_z \,. \tag{A.48}$$

First, consider the first equation with zero on the right-hand side,

$$\nabla^2 \pi_{z,g} + k_h^2 \pi_{z,g} = 0 \,. \tag{A.49}$$

If we assume $\pi_{z,g}$ in the form

$$\pi_{z,g} = \int_0^\infty D(z) \alpha J_0(\alpha\rho)\, d\alpha \,, \tag{A.50}$$

Equation (A.51) is easily obtained as

$$D(z) = Fe^{-\xi_h z} + Ge^{\xi_h z} \,. \tag{A.51}$$

The general solution $\pi_{z,g}$ is shown as

$$\pi_{z,g} = \int_0^\infty \left(Fe^{-\xi_h z} + Ge^{\xi_h z} \right) \alpha J_0(\alpha\rho)\, d\alpha \,. \tag{A.52}$$

Since we have known that

$$\pi_{z,p} = \frac{M_z}{4\pi\lambda}\frac{e^{ik_v s}}{s} = \frac{M_x}{4\pi\lambda}\int_0^\infty \frac{1}{\xi_v} e^{-\xi_v \lambda |z-z_0|} \alpha J_0(\alpha\rho) d\alpha \,, \tag{A.53}$$

It is easy to get the final solution of Equation (A.48) as

$$\pi_z = \frac{M_x}{4\pi\lambda}\int_0^\infty \left(\frac{1}{\xi_v} e^{-\xi_v \lambda |z-z_0|} + F e^{-\xi_h z} + G e^{\xi_h z} \right) \alpha J_0(\alpha\rho) d\alpha \,. \tag{A.54}$$